國 立 交 通 大 學

光 電 工 程 研 究 所

碩士論文

建構側邊鍍金波導管之表面電漿子 Fabry-Perot 量子點雷射

Plasmonic Quantum Dot Fabry-Perot Lasers With Sidewall-coated Metallic Waveguide

研究生：楊尚樺

指導教授：郭浩中 教授（NCTU）

盧廷昌 教授（NCTU）

中 華 民 國 九 十 八 年 六 月

建構側邊鍍金波導管之表面電漿子 Fabry-Perot 量子點雷射

Plasmonic Quantum Dot Fabry-Perot Lasers With Sidewall-coated Metallic Waveguide

研究生:楊尚樺   Student: Shang-Hua Yang

指導教授:郭浩中 教授   Advisor: Prof. Hao-Chung Kuo

盧廷昌 教授   Prof. Tien-Chang Lu

國 立 交 通 大 學
光 電 工 程 研 究 所
碩 士 論 文

A Thesis

Submitted to Institute of Electro-Optical Engineering

College of Electrical Engineering

National Chiao Tung University

in Partial Fulfillment of the Requirements

for the Degree of

Master

In

Electro-Optical Engineering

June 2009

Hsinchu, Taiwan, Republic of China

建構側邊鍍金波導管之表面電漿子Fabry-Perot量子點雷射

研究生：楊尚樺　　　　　　　　　　　　　　指導教授: 郭浩中教授

　　　　　　　　　　　　　　　　　　　　　　　盧廷昌教授

國立交通大學光電工程研究所碩士班

摘要

　　本論文中，我們主要研究以量子點(QD)作為活性介質(active medium)並其以側邊鍍金波導為結構的新型Fabry-Perot(FP)雷射，此雷射是由伊利諾大學香檳分校莊順連教授團隊呂建嶢所設計製造。除了元件結構設計和製成方法有詳盡介紹外，我們對此型量子點電漿子雷射做了完整的理論分析和靜態實驗量測並已觀察到雷射現象。我們以連續波模式(CW)和脈衝(pulsed)模式下，予電流灌注此雷射元件並觀測其放大自發輻射(ASE)頻譜。從實驗觀測放大自發輻射(ASE)頻譜數據，我們探知此FP雷射於1287奈米波段受激發光，並可從放大自發輻射中萃取淨模增益(net modal gain)、變折射率(refractive index change)、線寬增強因子(linewidth enhancement factor)和群折射率(group index)。從實驗分析，我們於雷射波段附近萃得約0.35的線寬增強因子。低線寬增強因子對於高頻操作、降低光絲線像(filamentation)、自我聚焦(selffocusing)、展區射極體的反導(antiguidance)和調變下頻率變化(chirp)有極大的幫助。此外。我們於攝氏7-15度區段取得無限大的特性溫度(characteristic temperature)，這表示完全溫度不敏感的元件操作是可行的。於量子點電漿子FP雷射所得高群速度顯示側邊鍍金屬層提供波導導引機制的色散影響。本碩論實驗結果顯示，此已可實現的側邊鍍金屬量子點電漿子FP雷射是擁有對稱增益、降低線寬增強因子、高溫度穩定度和於高頻操作下低頻率改變，並且對未來奈米雷射研究有程度上得幫助。

Plasmonic Quantum Dot Fabry-Perot Lasers With Sidewall-coated Metallic Waveguide
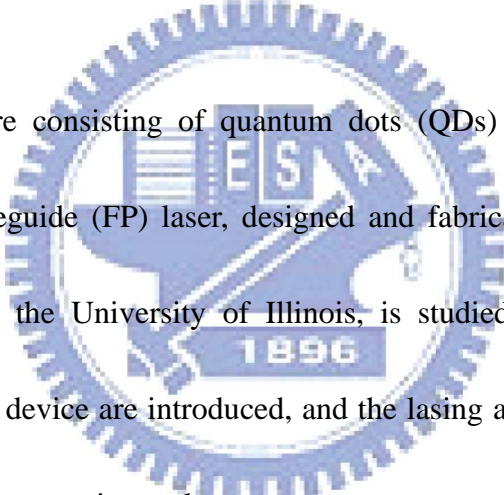
Student : Shang-Hua Yang   Advisor: Prof. Hao-Chung Kuo

Prof. Tien-Chang Lu

Institute of Electro-Optical Engineering

National Chiao Tung University

ABSTRACT

A new laser structure consisting of quantum dots (QDs) as the active medium and gold-coated metallic waveguide (FP) laser, designed and fabricated by Professor Chuang's group (Chien-Yao Lu) at the University of Illinois, is studied. Structure design and the fabrication method of this device are introduced, and the lasing action is also observed. Both theoretical analysis and experimental measurements are performed on the optical characteristics of the QD plasmonic laser. The amplified spontaneous emission (ASE) measurements of a QD plasmonic FP laser emitting in the 1287 nm wavelength region are investigated. Our experimental study of the ASE spectra under different injection currents includes both continuous wave (CW) and pulsed mode bias conditions. From the ASE spectra, we can extract the net modal gain, the refractive index change, the linewidth enhancement factor, and the group index. Our experimental analysis reveals a low linewidth enhancement

factor of about 0.35 at the lasing wavelength, which is helpful for high-speed operation, reduced filamentation, self-focusing, anti-guidance in broad-area emitters, and reduced chirp under modulation. Furthermore, we observed an infinite characteristic temperature T_0, in the range of 7-15°C, indicating completely temperature-insensitive operation is possible. The observed high group index in the QD plasmonic FP laser indicates that the sidewall-coated metal layers contribute to the dispersion of the waveguide guiding mechanism. Our experimental results show that the metallic sidewall-coated QD plasmonic FP laser is a promising device with symmetric gain, reduced linewidth enhancement factor, high temperature stability, which has considerable potential for future high-speed reduced-chirp operation, and helpful for plasmonic nanolaser studies.

ACKNOWLEDGMENTS

would like to thank to Chung Hwa Rotary Education Foundation for their scholarship support.

Most importantly, I would like to express the deepest gratitude to my parents Ho-Wen Yang and Hui-Hsiu Yu, and my girlfriend, Shih-Ting Huang, for their love, support and motivation.

CONTENT

LIST OF FIGURES

CHAPTER 1

INTRODUCTION

1.1 Motivation

The need to transmit signals optically is becoming increasingly apparent to improve data transportation rates to several gigabytes per second or even more. Fig. 1.1 shows the growth in information-carrying capacity of a single communication line. Such high rates are achieved by the modern techniques of microelectronic devices. Decades of research and investment in semiconductor development have brought today's high-end microprocessors that contain over 500 million transistors on a single chip. Fig. 1.2 plots the trend of the number of transistors in one chip. However, density of devices for optoelectronic devices on one single chip is far behind that of electronic devices due to the physical wavelength diffraction limitation, which prevents optoelectronics devices from further miniaturizing and it is an important issue that scientists need to overcome.

Recently, many researchers are interested in surface plasmon polaritons (SPPs) ranging from biologist, physicists, chemists and engineers. SPPs, also called plasmonics, are charge density waves on the surface of materials with free electrons propagating along the interface between a metal and a dielectric medium, as depicted in Fig 1.3. The advantages of plasmonics are the localization of electromagnetic modes
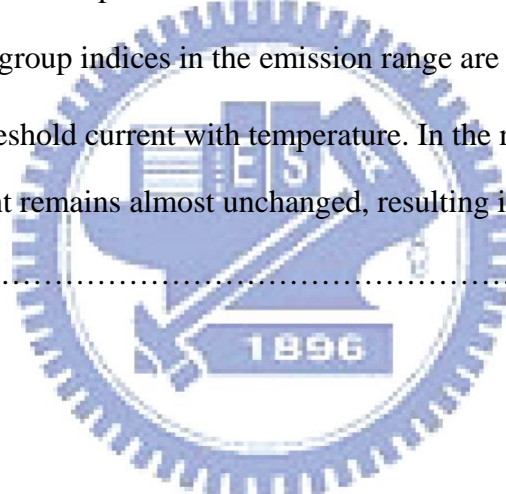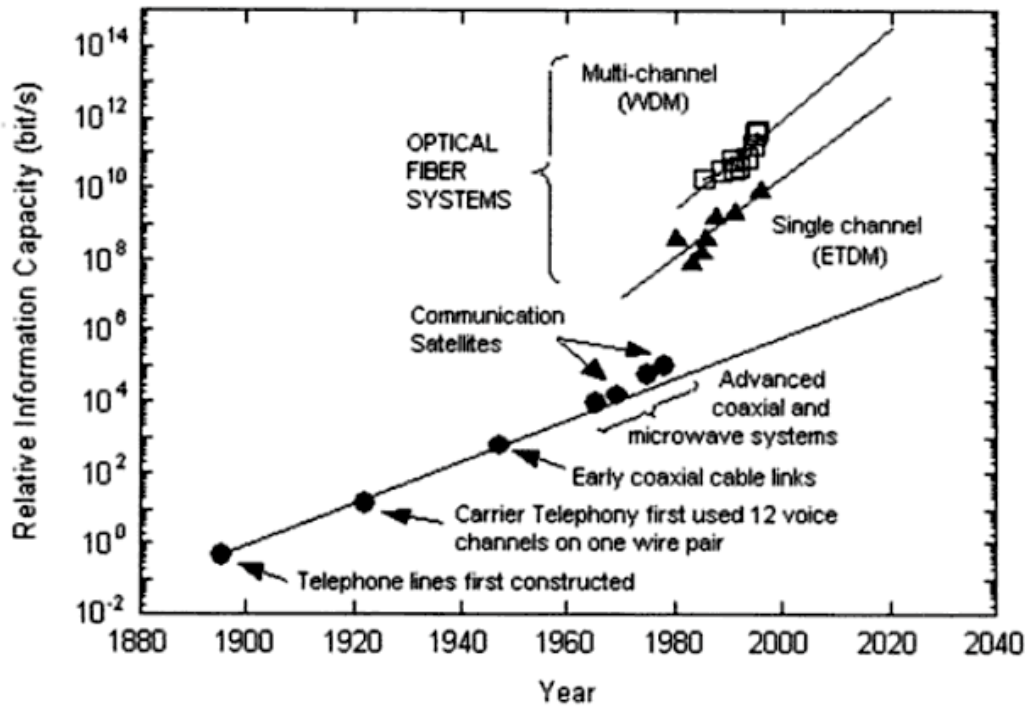
Fig 1.1 Growth in information carrying capacity of a single communication line [1]
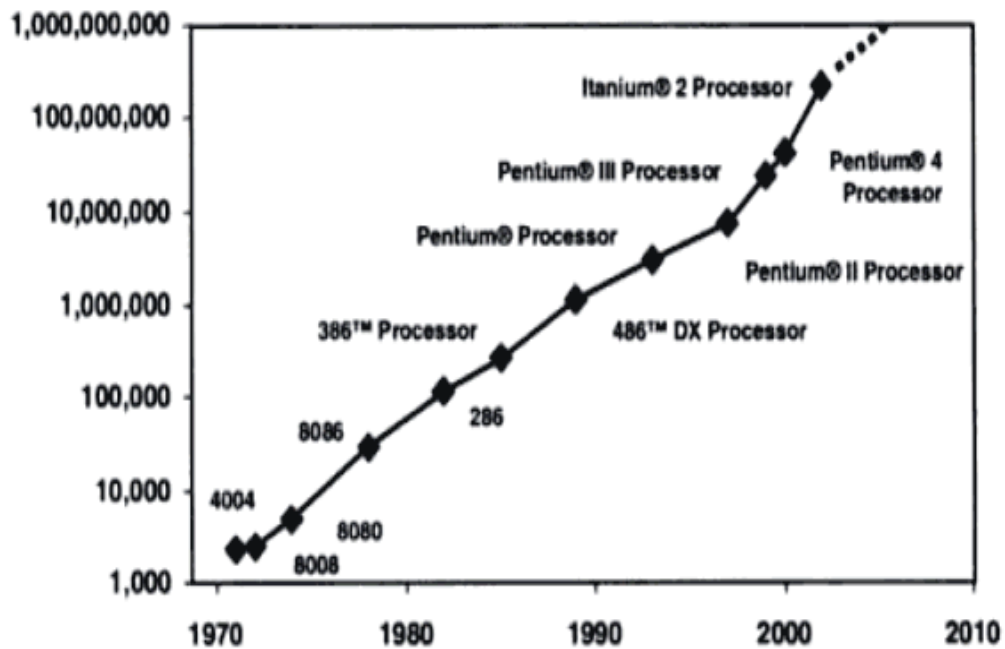
Fig 1.2 Number of transistors on a chip as a function of time since 1970. [1]

and capability of field enhancements. SPPs has been explored for their potential applications on bioimaging, microscopy, data storages, lithography, and nanolasers [2]. One of the most attractions from SPPs is concentrating and channeling light using subwavelength structures; hence, nano-scale photonic circuits are possibly achievable from this great advantage.

1.2   Applications of Plasmonic Subwavelength Technology

In bioimaging area, one of the most ultimate challenges is to realize behaviors of biomolecules in nature environments, that is, living cells. The cell functionality occurs at the nano-scale size region [5,6] which is not accessible by using classical techniques owing to diffraction limitation. Using conventional aperture type near-field scanning optical microscopy (NSOM), only a very small fraction of light on the order of $10^{-4} \sim 10^{-6}$ is detectable by using a 70 nm aperture which resolution is about 50 nm. Therefore, how to improve extraction efficiency of light from this tiny region becomes very critical for biosensing. On the other hand, metal planar nanostructure on glass stripes [7] has been demonstrated for its excellent ability to extract more than one thousand times emission intensity compared with that of the case without SPPs. Besides, same order of field enhancements using bowtie structure has been reported [8]. With significant improved emission from field enhancements, scientists can distinguish images in subwavelength range, which is almost impossible to achieve by using conventional method. Indeed, SPP is a promising technology to help the development in bioimaging area. Since the technique of biosensing and bioimaging are highly related to each other, SPP is also helpful for sensing a variety of target samples such as pesticides, pollutant, biological pathogens, toxins, and diseased tissue [9].

In order to integrate more devices in one chip, lots of effort have been made on fabricating nanoscale semiconductor devices to improve density of devices. However, without reliable

nanolithography techniques, nanoscale devices have difficulties to be integrated commercially. Although conventional maskless nanolithography, such as electron-beam and scanning probe lithography techniques, are reliable and can offer the desired flexibility [10], throughput is still too low to be commercially applied. Recently, by using an array of plasmonic lenses, which is put 20 nm above the surface of samples to be patterned, a linewidth of 80 nm has been demonstrated [11]. This method by applying plasmonic effects provides a new, low-cost, high-throughput approach to nanolithography techniques. This development would leads to a significant impact to the data storage industry as well as nanolithography.

1.3   Plasmonic Nanolaser

Plasmonics has recently been proposed as the strategy to further minimize size of semiconductor optoelectronic devices [2]. Metallic waveguides have been demonstrated with its better control over the confinement of the optical field [12], due to a large magnitude of the negative real part of the dielectric constant caused by surface plasma damping than conventional dielectric waveguides. Recently, because of the advance in the nanofabrication, the superb properties of the plasmonic cavity and waveguide have become an important issue. Novel nano devices with a resonant cavity smaller than the diffraction limit were fabricated and characterized by using the concept of plasmonics [13, 14]. Despite metals are lossy media, lasers with dimension smaller than the characteristic wavelength have been demonstrated and clear lasing action has been observed experimentally.

1.4   Organization of Thesis

The organization of this thesis is as follows. In Chapter 2, the physics of quantum dot lasers and optical waveguide theory will be introduced separately. We also present the theoretical comparison between non-metallic waveguides and metallic-coated waveguides to understand their fundamental differences. Theoretical results indicates group index of metallic waveguides behaves very differently from that of conventional dielectric waveguides. In Chapter 3, we present the fabrication and the structure of the quantum dot plasmonic laser. At the end of this chapter, we show the evidence for lasing action of this plasmonic device. In Chapter 4, we present theoretical and experimental studies on the net modal gain, refractive index change, linewidth enhancement factor, and group index of the quantum dot plasmonic Fabry-Perot laser. Our investigations includes both CW and pulsed current operations to distinguish the optical characteristics from thermal effects. In Chapter 5, we will summarize major achievements of this thesis and discuss further possible research.
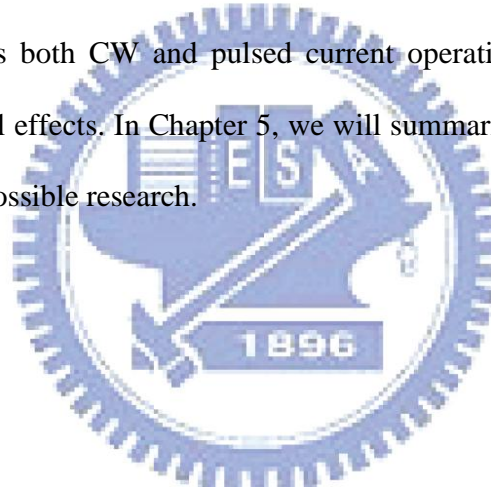
CHAPTER 2

PHYSICS OF QD FABRY-PEROT PLASMONIC LASER

2.1   QD Lasers

Effects of size quantization occurs when the size of confinement structures is comparable with de Broglie wavelength of carriers. In bulk semiconductor structures, carriers are free to move in all directions so that quantized effects do not occur. To restrict movement of one dimension of carriers, quantum well (QW) structure is proposed to confine carriers in planes perpendicular to the growth direction during layer-by-layer or Frank-Van der Merwe type of growth. By the end of 1980s, the technique of growing quantum wells and superlattices were well developed; hence, scientists in semiconductor area turned to investigate structures with less dimensionality - quantum wires and quantum dots (QDs). Quantum-wire material has a additional restriction along another dimensional to quantum quantum-well structure, and yields a 1-D semiconductor active layer. In addition to quantum-wire structure, QD structures can provide three-dimensional confinement for carriers and localize carriers in the QDs, which breaks down the classical model of a continuous dispersion of energy as a function of momentum. The comparison of the bulk (3-D), quantum well (2-D), quantum wire (1-D), and quantum dots (0-D) with associated density of states (DOS) are shown in Fig. 2.1. The resulting density of states of
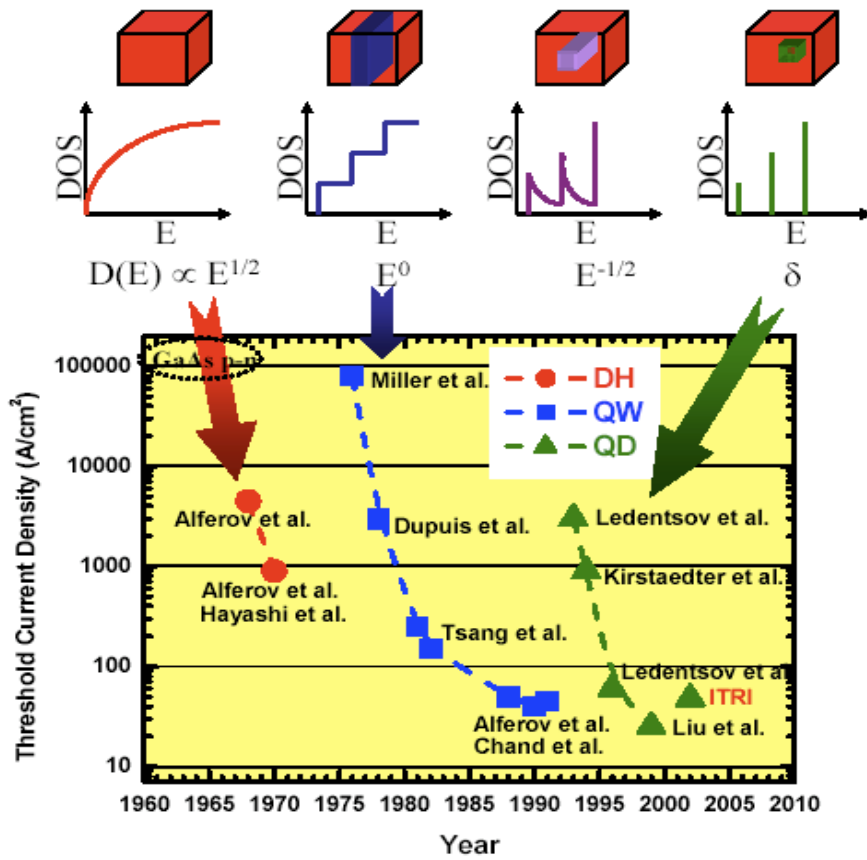
Fig 2.1 Physical structure and density of states for a bulk semiconductor, QW, Q-Wire, and QD structures. [15]

quantum dots are delta-function like and discrete, like in atomic physics. Therefore, the physical properties of quantum dot structures respected resemble an atom in a cage. Fig. 2.2 shows the size comparison between bulk, quantum dots and atoms.

The most attracting property of QDs is its completely discrete transition energy level because of the delta-function-like density of states. Therefore, if we use QDs as gain medium to fabricate lasers, carriers can be efficiently utilized because of the delta-function-like density of states. Thus, the threshold gain is easy to reach by effectively using usage of injecting carriers.

Macroscopic	Wavelength of light	De Broglie Wavelength at 300K	
Volume Semiconductor	Waveguide	Quantum Dot	Atom
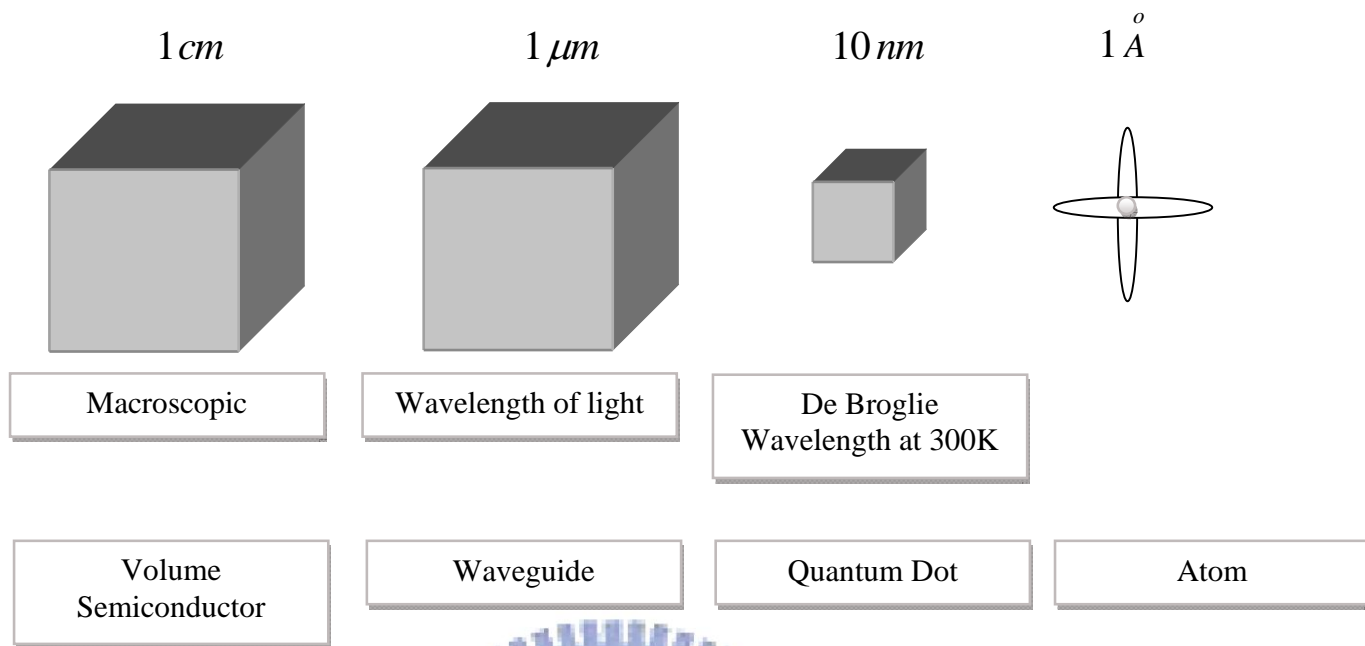
Fig 2.2 Schematic comparison of typical dimensions of bulk material, waveguide for visible light, quantum dots, and atoms.

Hence, QD lasers feature ultra low threshold density and ultrahigh temperature threshold stability, which are two of the main advantages over conventional QW lasers or bulk lasers [16,17]. The lasing spectra stability with temperature and ultra high differential gain are also guaranteed by the sharp gain spectrum of QDs.

The first concept of QD semiconductor laser was proposed by Dingle and Henry in 1976 [18] and later by Arakawa and Sakaki in 1982 [17]. Experimentally, the growth of QDs had been realized by the self-organized Stranski-Krastanov (S-K) growth method, as shown in Fig 2.3. The S-K method can be carried out by using either metal-organic chemical vapor deposition (MOCVD) or molecular beam-epitaxy (MBE) growth method. However, size and shape of QDs fabricated by the S-K method fluctuate randomly, resulting in the inhomogeneous broadening in
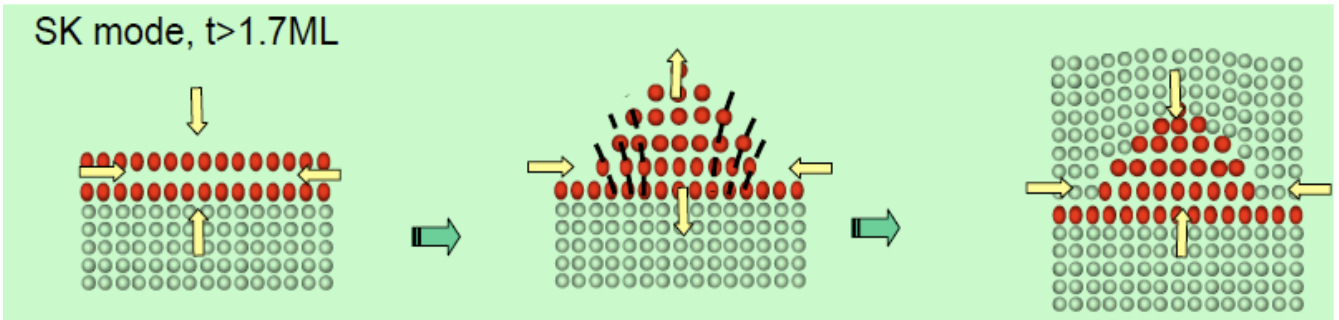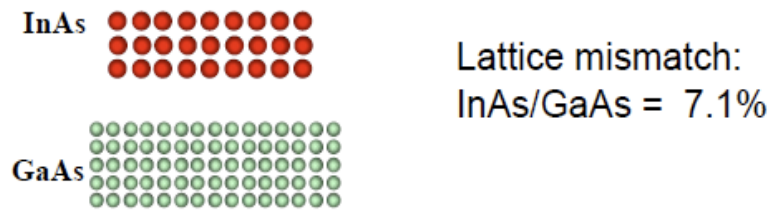
Fig 2.3 Stranski-Krastanov (SK: layer-plus-island) mode of thin film growth. [19]

gain spectrum. This real situation would induce temperature dependence of threshold properties and broaden linewidth of laser devices.

2.2   Optical Waveguide Theory

In order to understand fundamental differences between dielectric and metallic waveguides, this section presents 1-D model for both dielectric and metallic waveguides. Numerical examples are also given to compare their difference on group index.

Dielectric Slab Waveguide [20]

Consider a slab waveguide as shown in Fig. 2.4. From the wave equation [20],

$$(\nabla^2 + \omega\mu\varepsilon)\vec{E} = 0 \tag{2.1}$$
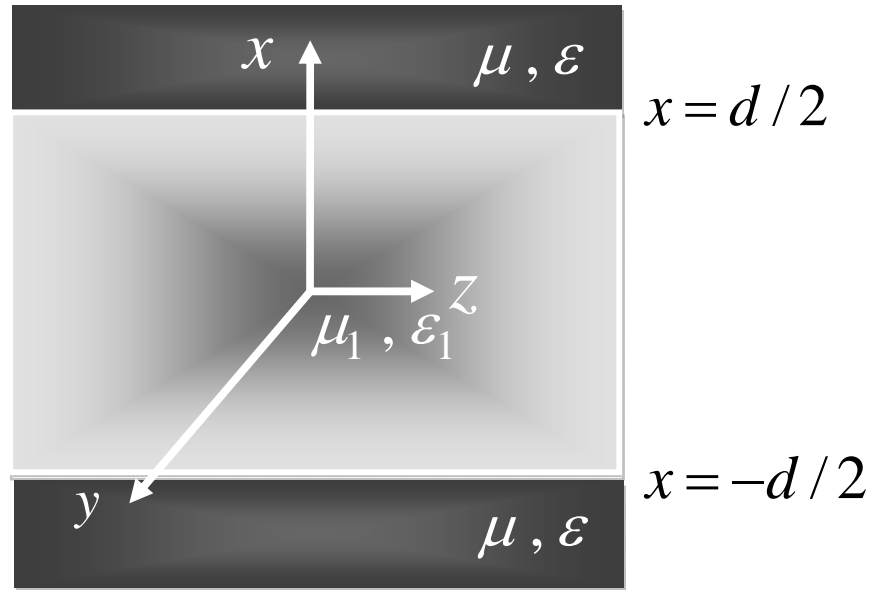
Fig 2.4 A simple slab waveguide structure for waveguide analysis.

the electric field can be solved. We assume the structure is symmetric waveguide and the waveguide width w is far larger than the thickness d; hence the field dependence on y direction is negligible. The permittivity and permeability of the cladding layers are ε and μ, respectively. The permittivity and permeability of the waveguide are ε_1 and μ_1, respectively. We assume $n_1(=\dfrac{\omega\sqrt{\mu_1\varepsilon_1}}{k_0})$ is larger than $n(=\dfrac{\omega\sqrt{\mu\varepsilon}}{k_0})$.

Since both TE and TM polarized light exist in the waveguide, we first consider only TE-polarized light modes of the waveguide. After the TE modes are obtained, TM modes can be easily obtained by using the duality principle [18].

For TE polarization, the electric field of the even modes can be written

$$E_y = e^{ik_z z} \begin{cases} C_0 e^{-\alpha(x-d/2)} & x \geq \dfrac{d}{2} \\[2mm] C_1 \cos k_x x & |x| \leq \dfrac{d}{2} \\[2mm] C_2 e^{+\alpha(x+d/2)} & x \leq -\dfrac{d}{2} \end{cases}$$

(2.2)

By substituting Eq. (2.2) into Eq. (2.1), we obtain

$$k_x^2 + k_z^2 = \omega^2 \mu_1 \varepsilon_1$$
$$-\alpha^2 + k_z^2 = \omega^2 \mu \varepsilon$$

(2.3)

After manipulation for Eq. (2.3), we get

$$k_x^2 + \alpha^2 = \omega^2 (\mu_1 \varepsilon_1 - \mu \varepsilon)$$

(2.4)

Where $e^{ik_z z}$ stands for the guided waves propagate in the $+z$ direction, α is the decay constant in the cladding layer, and $\cos k_x x$ is chosen to be the standing wave solution. From the boundary condition, we can get

$$C_0 = C_1 \cos \left(k_x \frac{d}{2} \right)$$
$$\frac{\alpha}{\mu} C_0 = C_1 \frac{k_x}{\mu_1} \sin \left(k_x \frac{d}{2} \right)$$

(2.5)

By manipulating Eq. (2.5), we have

$$\alpha = \frac{\mu}{\mu_1} k_x \tan \left(k_x \frac{d}{2} \right)$$

(2.6)

From Eq. (2.4) and Eq. (2.6), one can solve k_z and α. As the decay constant α and propagation constant k_z are solved, the normalize parameters C_0, C_1, C_2, can be obtained. Than, the electric and magnetic wave of the TE even modes in this structure are well analyzed. On the other hand, the electric field for the odd modes for TE-polarized light can be written as

$$E_y = e^{ik_z z} \begin{cases} C_0 e^{-\alpha(x-d/2)} & x \geq \dfrac{d}{2} \\[2ex] C_1 \sin k_x x & |x| \leq \dfrac{d}{2} \\[2ex] C_2 e^{+\alpha(x+d/2)} & x \leq -\dfrac{d}{2} \end{cases} \tag{2.7}$$

From the boundary condition, we have

$$C_0 = C_1 \sin (k_x \frac{d}{2}) \tag{2.8a}$$

$$-\frac{\alpha}{\mu} C_0 = C_1 \frac{k_x}{\mu_1} \cos (k_x \frac{d}{2}) \tag{2.8b}$$

By manipulating Eq. (2.8a) and Eq. (2.8b), we obtain

$$\alpha = -\frac{\mu}{\mu_1} k_x \cot (k_x \frac{d}{2}) \tag{2.9}$$

Using the same procedures, electromagnetic waves in this structure can be obtained.

For TM polarization, we can apply the duality principle into the above equations: replacing the field solution E and H by H and -E, respectively, and the permittivity and permeability change the symbol to each other.

The effective index and group index for the guided mode are expressed as

$$n_{eff} = \frac{k_z}{k_0} \tag{2.10}$$

$$n_g = n_{eff} - \lambda \frac{\partial n_{eff}}{\partial \lambda} \tag{2.11}$$

where k_0 is the wave vector in the free space. Since $\dfrac{\omega\sqrt{\mu\varepsilon}}{k_0} = n$ and $\dfrac{\omega\sqrt{\mu_1\varepsilon_1}}{k_0} = n_1$ are given

parameter, the effective index $n_{eff}(\lambda)$ should falls in the region of $n(\lambda) < n_{eff}(\lambda) < n_1(\lambda)$ when

the material dispersion is taken into account.

Surface Plasmon Waveguide [18]

The surface Plasmon waveguide theory follows Professor Chuang's book, second edition [18]. The permittivity of the metal can be expressed as

$$\varepsilon_p(\omega) = \varepsilon_0 (1 - \frac{\omega_p^2}{\omega^2})$$

(2.12)

where ω_p is the plasma frequency and ε_0 is the vacuum permittivity. In the range of optical frequency, the permittivity of the metal becomes negative since optical frequency is far smaller than plasma frequency and leads to a significant field attenuation when electromagnetic waves propagate in metal.

Consider a thin metallic slab waveguide as shown in Fig. 2.5. We assume the structure is a symmetric waveguide and the waveguide width w is far larger than the thickness d; hence the field dependence on y direction is negligible. The permittivity of the dielectric medium and metal are ε_1 are ε_p, respectively.

For TM polarization, the magnetic field for the even mode can be written as

$$H_y = e^{ik_z z} \begin{cases} C_0 e^{-\alpha_1(x-d/2)} & x \geq \dfrac{d}{2} \\[2mm] C_1 \cosh \alpha_2 x & |x| \leq \dfrac{d}{2} \\[2mm] C_0 e^{+\alpha_1(x+d/2)} & x \leq -\dfrac{d}{2} \end{cases}$$

(2.13)

Substituting Eq. (2.13) into Eq. (2.1) gives

$$-\alpha_1^2 + k_z^2 = \omega^2 \mu \varepsilon_1$$
$$-\alpha_2^2 + k_z^2 = \omega^2 \mu \varepsilon_p$$

(2.14)
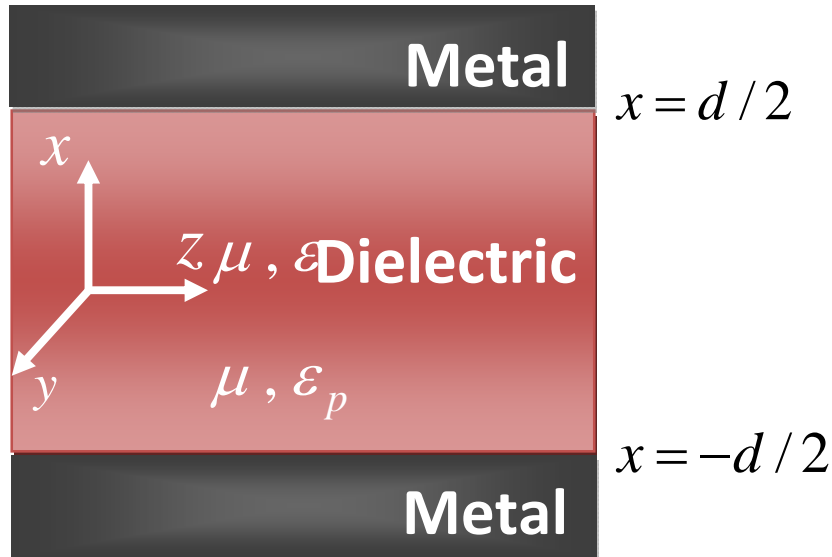
Fig 2.5 A metallic slab waveguide structure for waveguide analysis.

where α_1 and α_2 are decay constant in the dielectric and metal, respectively. From the boundary conditions, we obtain

$$C_0 = C_1 \cosh\left(\alpha_2 \frac{d}{2}\right)$$

$$-\frac{\alpha_1}{\varepsilon_1} C_0 = C_1 \frac{\alpha_2}{\varepsilon_p} \sinh\left(\alpha_2 \frac{d}{2}\right)$$

$$(2.15)$$

Thus, manipulating Eq. (2.15) gives

$$\alpha_1 = -\frac{\varepsilon_1}{\varepsilon_p} \alpha_2 \tanh\left(\alpha_2 \frac{d}{2}\right)$$

$$(2.16)$$

From Eq. (2.14) and Eq. (2.16), one can solve the decay constant α_1 and α_2. Then, the other parameters k_z, C_0, C_1 can also be obtained.

For TM polarization, the magnetic field for the odd modes can be written as

$$H_y = e^{ik_z z} \begin{cases} C_0 e^{-\alpha_1 (x-d/2)} & x \geq \dfrac{d}{2} \\[2mm] C_1 \sinh \alpha_2 x & |x| \leq \dfrac{d}{2} \\[2mm] C_0 e^{+\alpha_1 (x+d/2)} & x \leq -\dfrac{d}{2} \end{cases} \tag{2.17}$$

From the boundary conditions, we have

$$C_0 = C_1 \sinh\left(\alpha_2 \frac{d}{2}\right)$$

$$-\frac{\alpha_1}{\varepsilon_1} C_0 = C_1 \frac{\alpha_2}{\varepsilon_p} \cosh\left(\alpha_2 \frac{d}{2}\right) \tag{2.18}$$

By manipulating Eq. (2.18), we have

$$\alpha_1 = -\frac{\varepsilon_1}{\varepsilon_p} \alpha_2 \coth\left(\alpha_2 \frac{d}{2}\right) \tag{2.19}$$

Using the same procedure, electric and magnetic fields in this structure can be obtained.
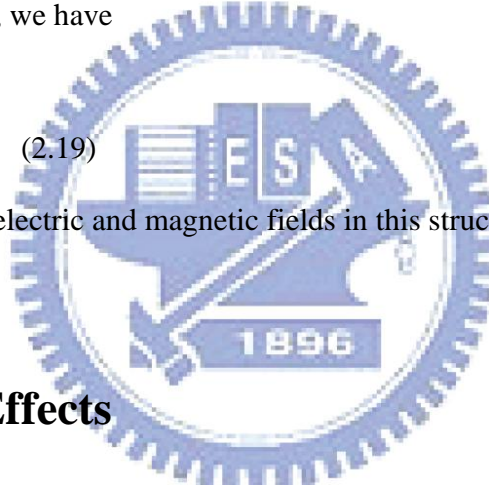
2.3　Plasmonic Effects

Group index is a good property to investigate plasmonic effects. To see clear difference of group index between dielectric and metallic waveguides, we consider a slab $Al_{0.35}Ga_{0.65}As / GaAs / Al_{0.35}Ga_{0.65}As$ waveguide and a slab Au/GaAs/Au metallic waveguide with identical waveguide width w.

In Fig 2.6, we plot the effective refractive index $n_{eff}(\lambda)$ of the TM even mode versus wavelength of a slab $Al_{0.35}Ga_{0.65}As / GaAs / Al_{0.35}Ga_{0.65}As$ waveguide. The waveguide width w is set as 50 nm. The material dispersion is considered in the simulation.
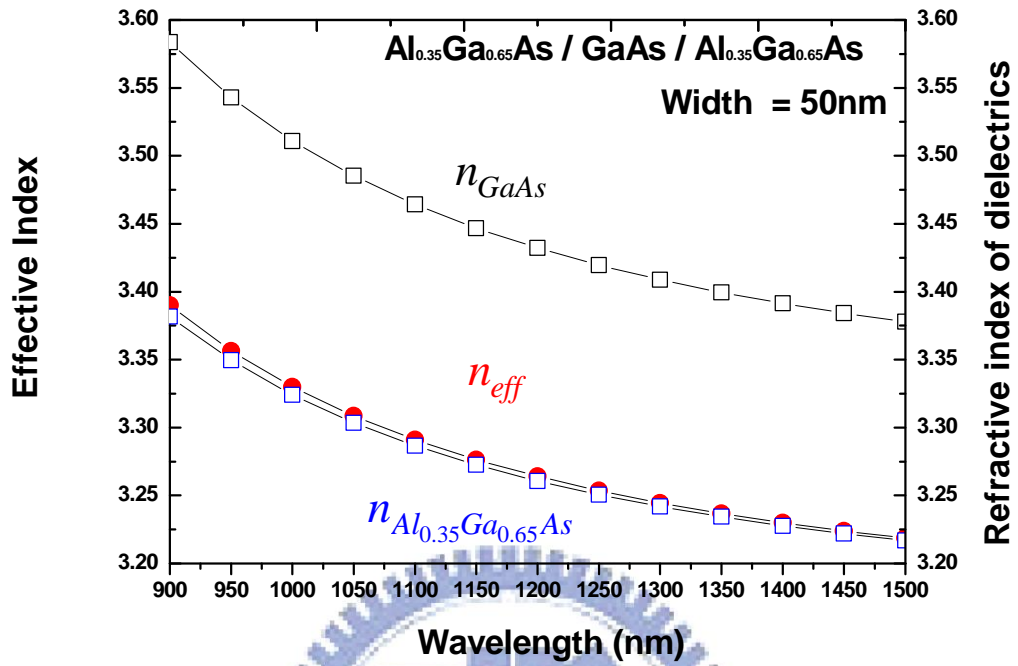
Fig 2.6 Simulation results of the effective refractive index $n_{eff}(\lambda)$ versus wavelength of a slab $Al_{0.3}Ga_{0.7}As/GaAs/Al_{0.3}Ga_{0.7}As$ waveguide.

Fig 2.7 shows the numerical results of the group index $n_g(\lambda)$ versus wavelength of a slab $Al_{0.35}Ga_{0.65}As/GaAs/Al_{0.35}Ga_{0.65}As$ waveguide obtained from Eq. (2.11). It is clear to see the value of group index falls between the refractive index of $GaAs$ and the refractive index of $Al_{0.35}Ga_{0.65}As$. In Fig 2.8, we plot the TM even mode of effective refractive index $n_{eff}(\lambda)$ versus wavelength of a plasmonic $Au/GaAs/Au$ waveguide. The structure of the width w is set as the same number, 50nm, and the permittivity of gold is -14.8.
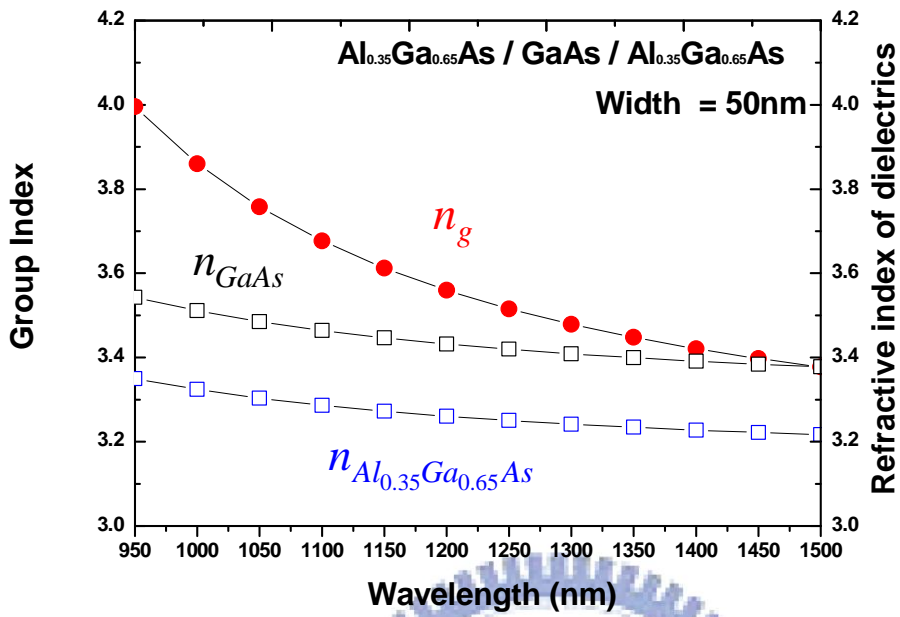
Fig 2.7 Simulation results of the group index $n_g(\lambda)$ versus wavelength of a slab $Al_{0.35}Ga_{0.65}As / GaAs / Al_{0.35}Ga_{0.65}As$ waveguide.
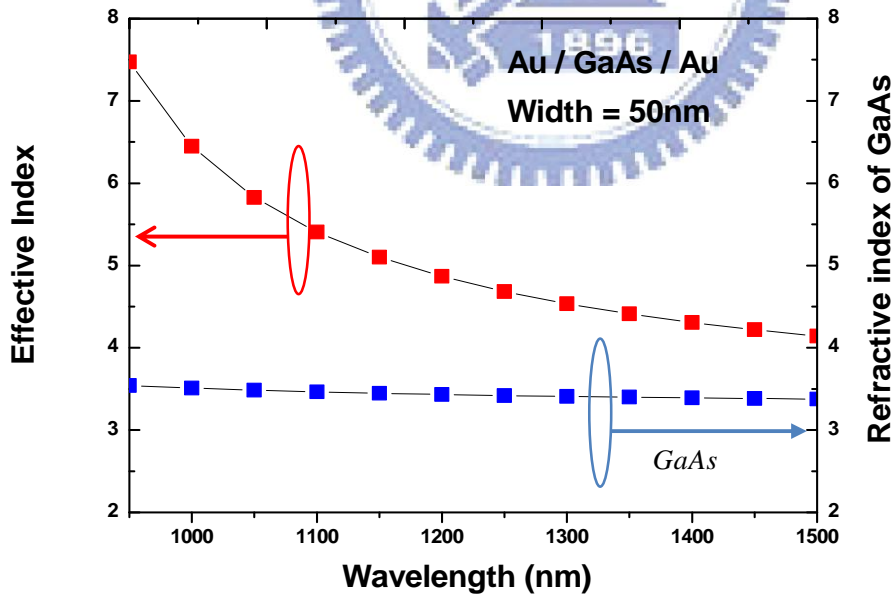
Fig 2.8 Simulation results of the effective refractive index $n_{eff}(\lambda)$ versus wavelength of a $Au / GaAs / Au$ plasmonic waveguide.
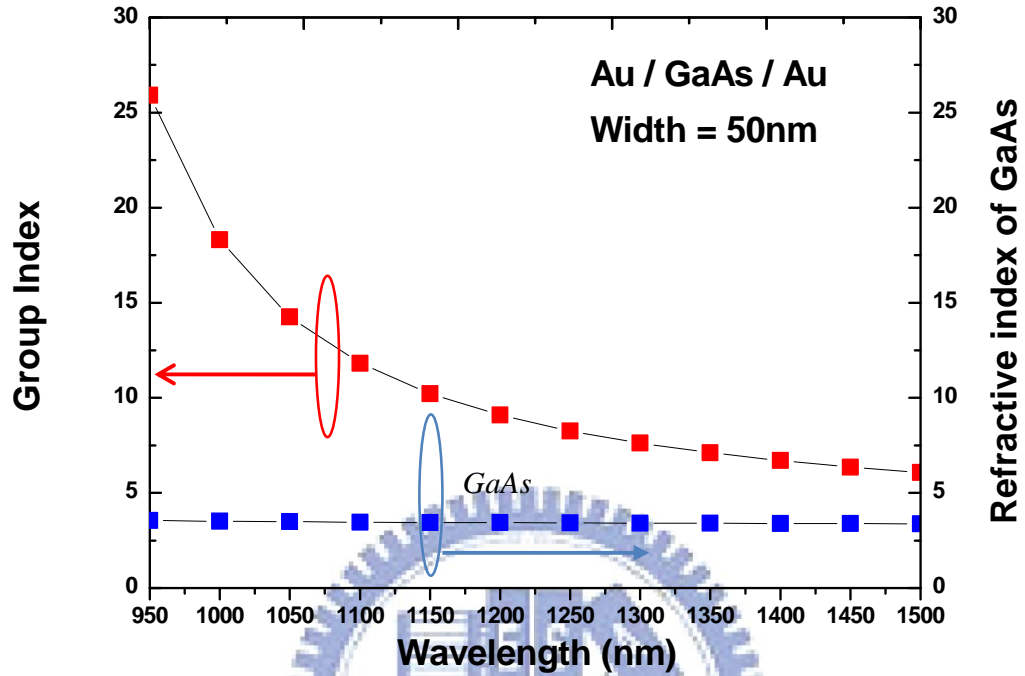
Fig 2.9 Simulation results of the group index $n_g(\lambda)$ versus wavelength of a $Au/GaAs/Au$ plasmonic waveguide.

Fig 2.9 shows the group index $n_g(\lambda)$ versus wavelength of the slab plasmonic waveguide, which can be obtained from Eq. (2.11). It is clear to see the group indices are larger than that of $GaAs$. This means that plasmonic effects modify the dispersion relation of the guided modes resulting in an extremely high group index.

2.4   Conclusion

We has described the fundamental properties of 3-D (bulk), 2-D (quantum well), 1-D (quantum wire), and 0-D (quantum dot) materials. The main advantages of the QD lasers over QW lasers and bulk lasers are ultra low threshold density, temperature insensitivity, discrete energy levels, and delta-like shape density of states. Furthermore, the optical waveguide theory for dielectric waveguide and metal-semiconductor-metal waveguide is derived to understand the fundamental difference between the two types of waveguide. The given numerical examples for comparison between dielectric and metallic waveguide indicates that the group index will be increased when plasmonic effects affect the guided modes.
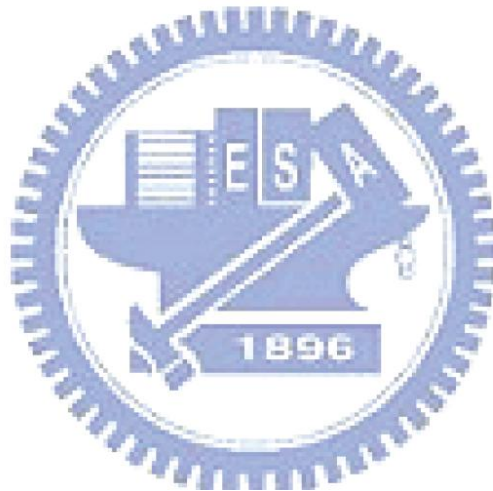
CHAPTER 3

QD PLASMONIC LASER GROWTH, STUCTURE, AND LASING ACTION

In this chapter, we present the design structure and fabrication of a QD with sidewall-coated metallic waveguide. The luminescence is also included in the content. Despite metals are lossy media, we observed clear lasing action and a low threshold density current.

3.1   Structure and Growth

Fig. 3.1 shows the cross section of the fabricated QD plasmonic laser by Chien-Yao Lu in Professor Chuang's group at the University of Illinois. A series of Fabry-Perot lasers were fabricated with the sample containing InAs/GaAs quantum dots as the active medium. Ten stacks of QD layer are sandwiched between $1.5\,\mu m$ thick $Al_{0.35}Ga_{0.65}As$ cladding layers and covered with a 5-nm-thick $In_{0.15}Ga_{0.85}As$ quantum-well cap layer [21]. A 500 nm SiN_x layer was deposited by plasma-enhanced chemical vapor deposition and was then patterned by photolithography to define the dry etching mask for the ridge waveguides. Inductive coupled plasma reactive ion etching (ICP-RIE) technique was used to produce a $2\,\mu m$ deeply-etching ridge waveguide with vertical sidewalls. A thin SiN_x passivation layer serving as the
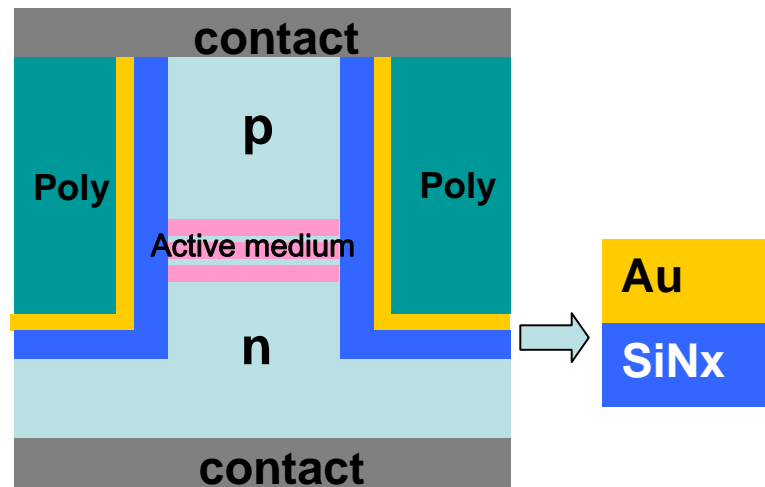
Fig 3.1 The cross section structure of the fabricated QD plasmonic laser. The device was fabricated by Chien-Yao Lu in Professor Chuang's group at the University of Illinois.
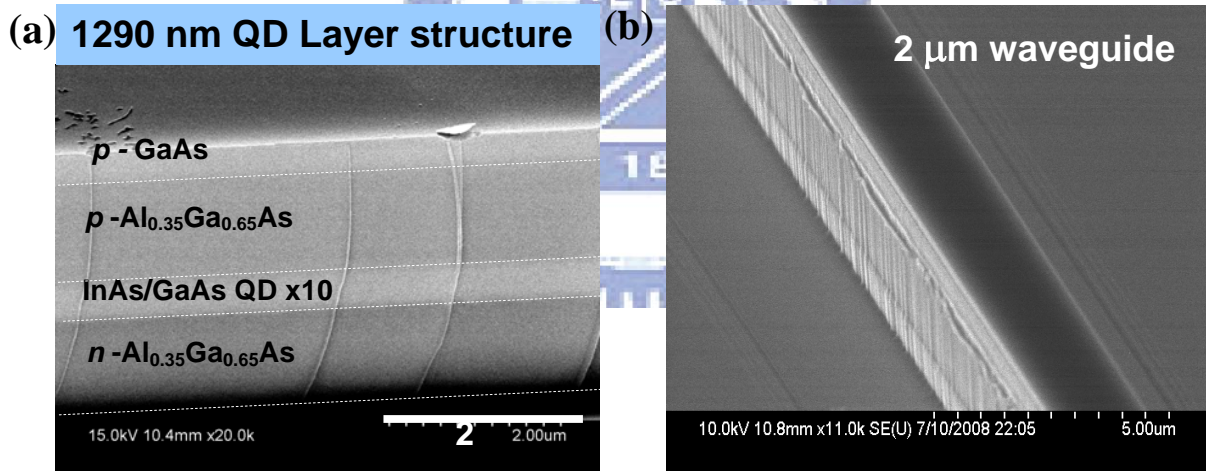
Fig 3.2 SEM image of the waveguide. (Photos taken by C. Y. Lu at UIUC).

electrical isolator was then deposited on the sidewall followed by a conformal metallic coating (100 nm Au / 5 nm Ti). Fig 3.2 shows the scanning electron microscope (SEM) image of the waveguide cross section view. The whole sample was lapped down to about 100 μm to allow

the easy cleaving of device facets before the deposition of the n-type contacts on the backside of the sample. The sample was then cleaved to several devices with various waveguide lengths.

3.2   Lasing Action

The laser device was mounted on the copper heat sink by indium and conductive epoxy for the measurements. The device was operated at 293 K under DC current operation with a fiber tip to collect the emitted light from the device. The device temperature was kept constant by thermo-electric cooler (TEC) with feedback control signal from the thermal couple sensor. Fig. 3.3 shows our experimental setup for measuring the steady-state light emission of the QD plasmonic laser. The current source (ILX LDC-3900) and TEC controlled via Labview program are used to drive and sustains the temperature of the plasmonic QD laser. The optical power meter is used to collect light emission for intensity analysis and also can be controlled by Labview program. Fig. 3.4 shows the control front panel of the Labview program. We use both lens-fiber and fiber tip to collect light from the device. The fiber tip has a better ability to extract light from the facet of the plasmonic laser than the lens-fiber. However, lens fiber has the advantage of reducing feedback and eliminate the external cavity effects. Fig. 3.5 (a) shows the plot of emission intensity versus different injection current (L-I curve) and Fig. 3.5 (b) shows the voltage versus different injection current (I-V curve) of the 1150-μm-long laser device, respectively. A clear onset of LI curve is evident for lasing action.

Fig. 3.6 shows our experimental setup for measuring the amplified spontaneous emission of the QD plasmonic laser in steady state. The same current source is used to drive the plasmonic
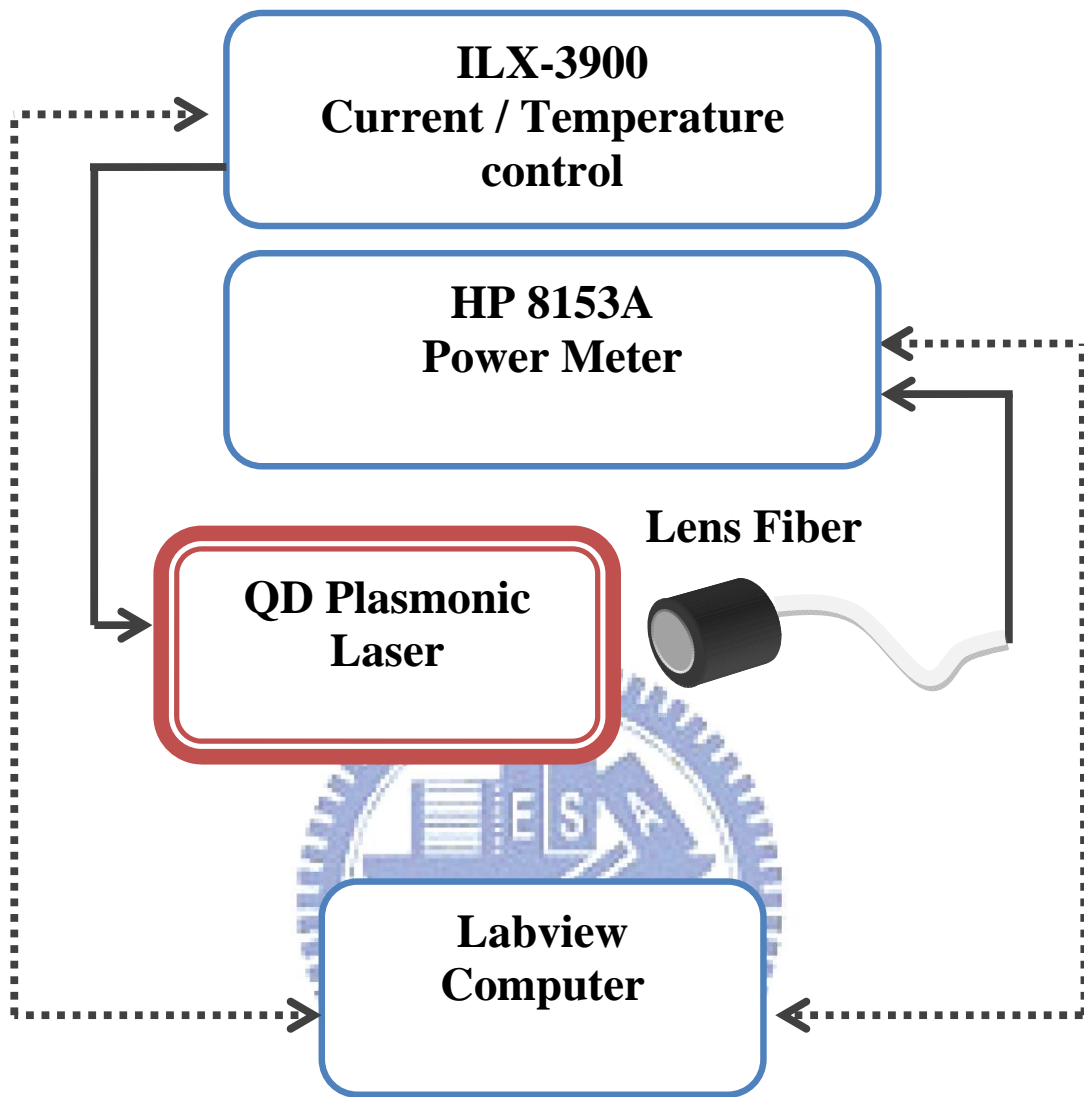
Fig 3.3 The diagram of the experimental setup used in obtaining the steady-state light emission of the QD plasmonic laser.

QD laser controlled via global parallel interface bus (GPIB) computer surface and it can be precisely operated to μA level. The TEC also sustains the temperature of the QD plasmonic laser which is mounted on the copper heat-sink stage and set in the current controlled device steering by the GPIB interface. Fig. 3.7 shows the vi. of Labview program that we use for the
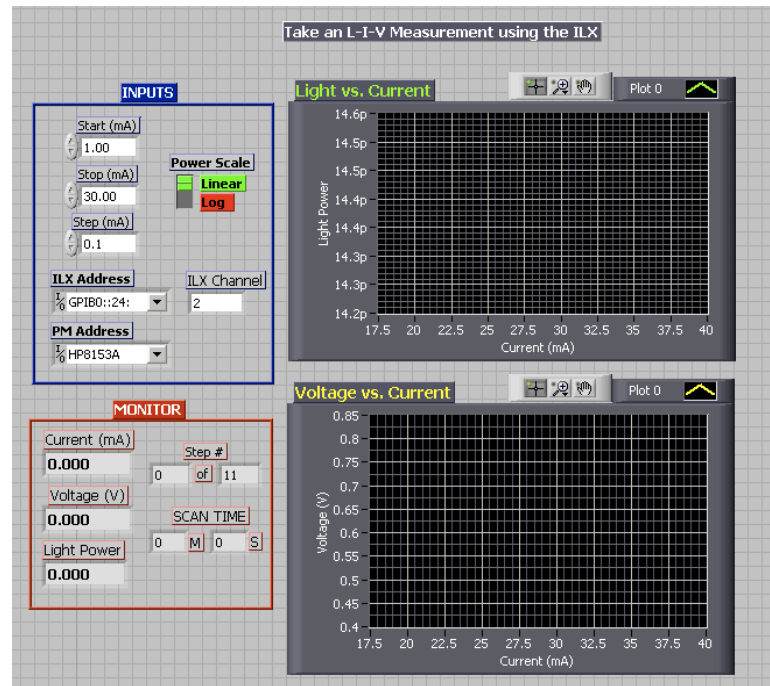
Fig 3.4 Schematic of LIV measurement by using Labview control front panel
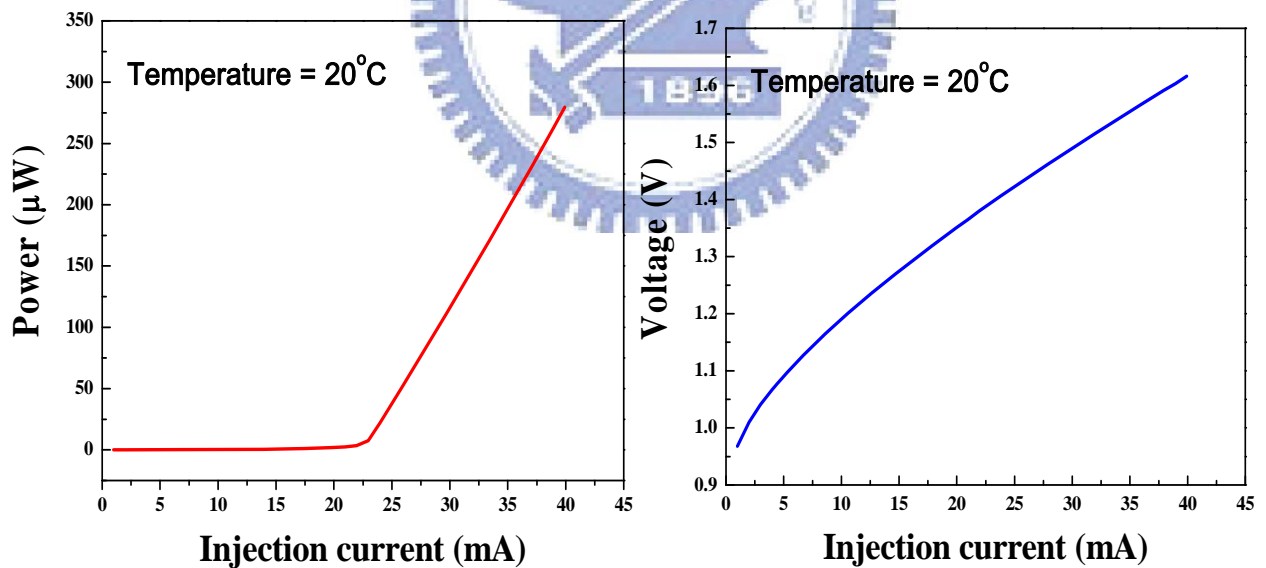
Fig 3.5 (a) Emission intensity versus different injection current (L-I curve) of the QD plasmonic

laser. (b) Voltage versus different injection current (I-V curve) of the QD plasmonic laser.

experiment. The Optical Spectrum Analyzer (OSA) is used to collect light emission for spectrum analysis and can be controlled by Labview program. The resolution of OSA (ADVANTEST Q8347) can be down to 5.7 pm and sensitivity has the limitation to -95dBm. The fiber shown in Fig. 3.8 is manufactured by balled lens fiber type using fusion splicing technique. This designed setup reduces feedback and eliminates the external cavity effects of conventional methods. Moreover, it improves the coupling efficiency of collecting light from the device under test.
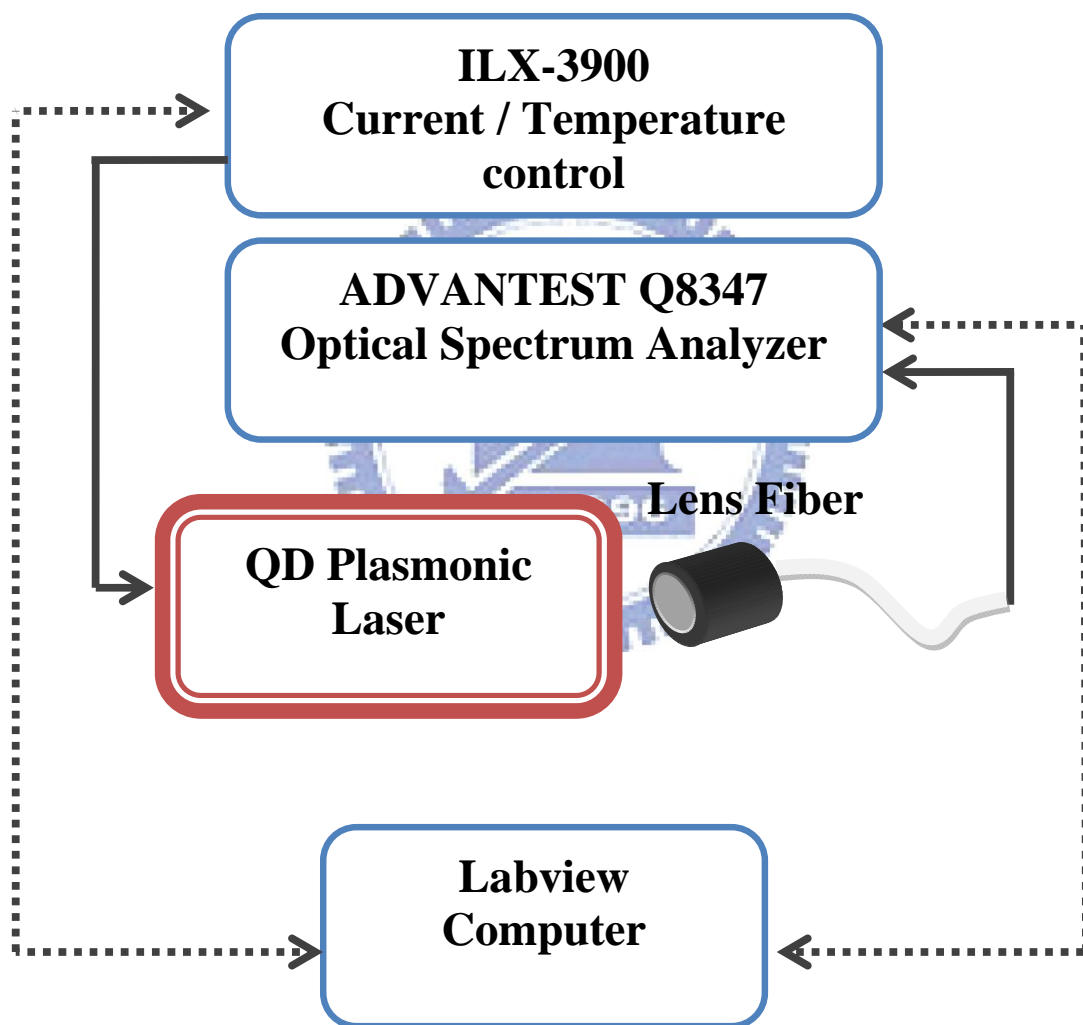
Fig 3.6 The diagram of the experimental setup used for obtaining the ASE spectrum from the QD plasmonic laser.
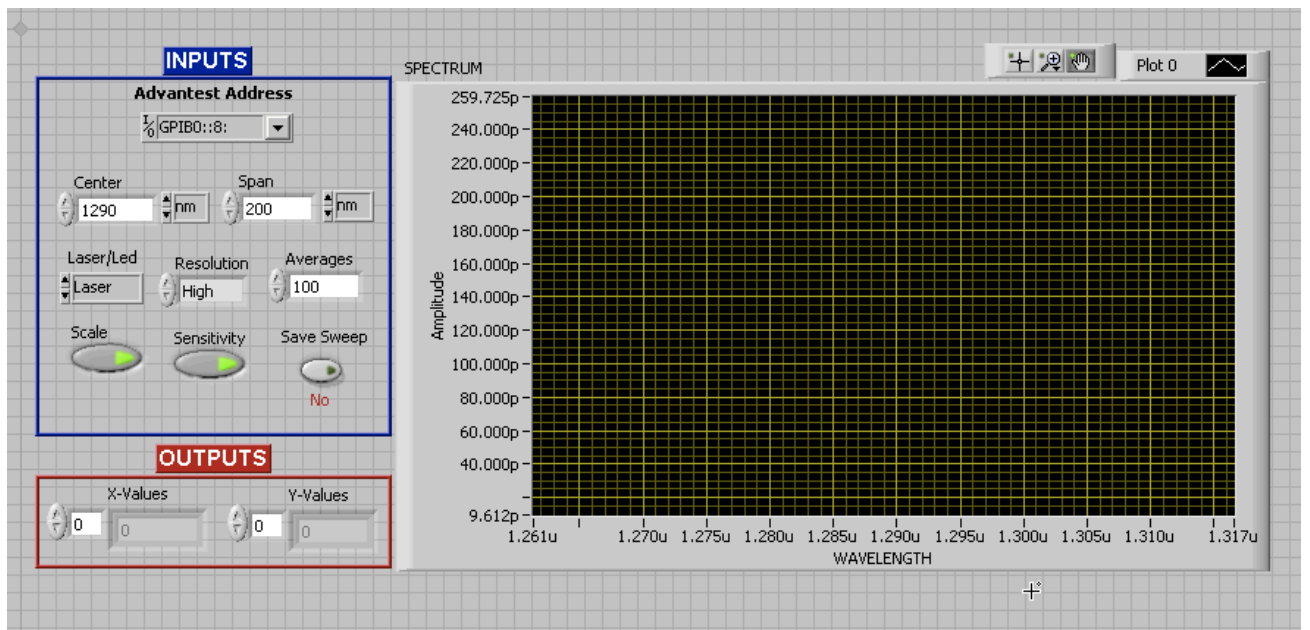
Fig 3.7 Schematic of ASE spectrum measurement by using Labview control front panel

Injecting carrier (by probe)

Lens Fiber

Plasmonic QD FP Laser
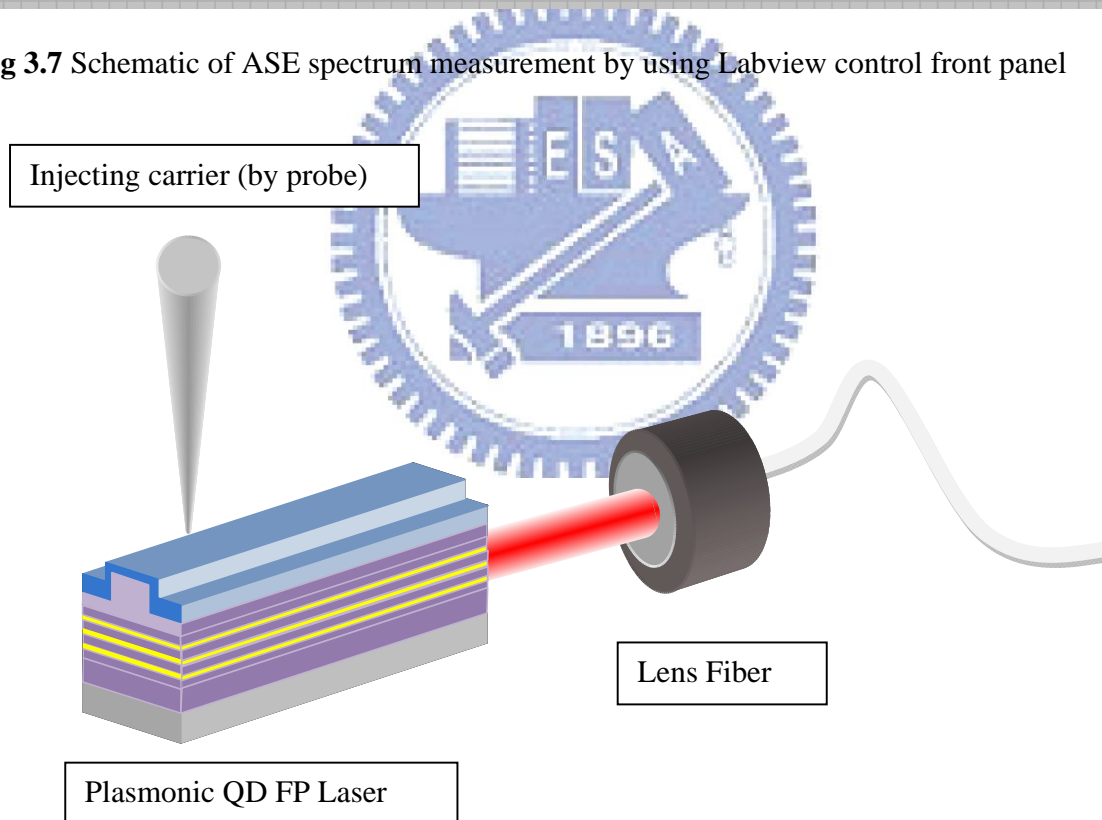
Fig 3.8 The amplified spontaneous emission is collected by lens fiber from the facet of our

plasmonic QD Fabry-Perot laser

The amplified spontaneous emission is collected from the facet of our plasmonic QD Fabry-Perot laser, lens fiber, and finally showed on the OSA screen. The laser device is p-side up. We use Scanning Electron Microscope (SEM) to precisely measure the device length, which is 1150 μm. By the means of Labview program, setup control and data analysis on the computer is also available.
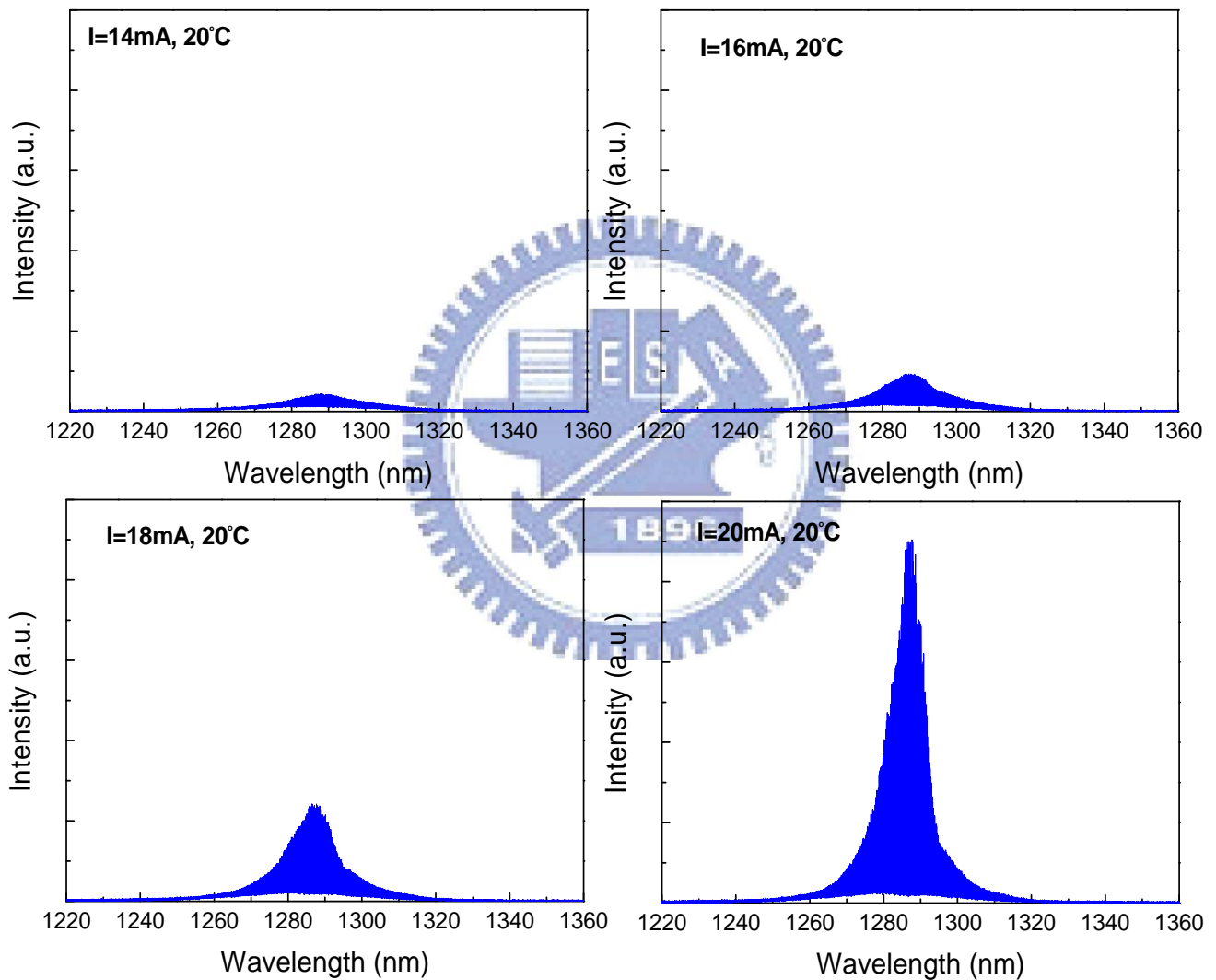
Fig 3.9 Amplified spontaneous emission under different injection currents (below threshold) from the QD plasmonic laser.

Fig. 3.19 shows the optical spectrum emission under different injected currents below threshold. For the spectrum below threshold, clear amplified spontaneous emission is observed and the clear interference pattern in the spectrum is owing to the Fabry-Perot resonance. As the injected current is larger than the threshold current, stimulated emission takes place and leads to lasing action. The clear resonance peak at 1287nm is depicted in Fig. 3.9. The main lasing wavelength is about 1287 nm, as shown in Fig 3.10. A clear onset of significant stimulated emission is observed. As is shown in Fig. 3.9, the threshold current of the device is about 22.5mA. Corresponding to a threshold current density is 0.978 kA/cm^2 [12], which is comparable to or even lower than typical quantum well semiconductor lasers.
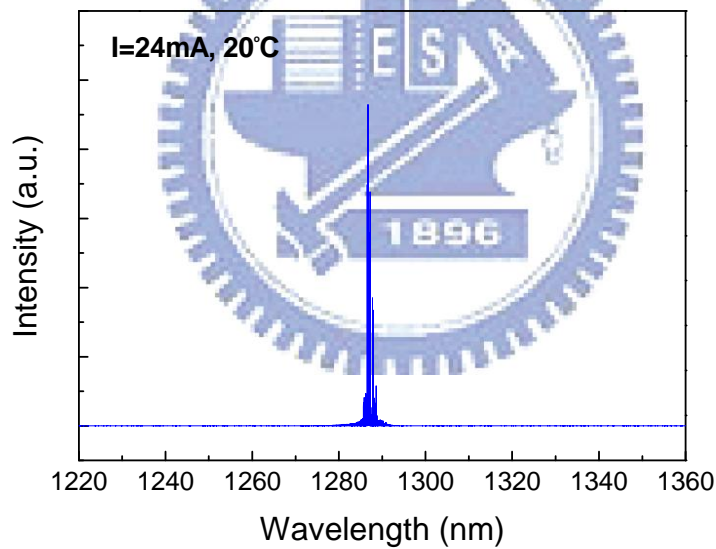
Fig 3.10 Spectrum of QD plasmonic laser biased at 24mA (above threshold).

CHAPTER4

DC CHARACTERISTICS OF FABRY-PEROT

PLASMONIC LASER

4.1   Introduction

In this chapter, we describe the theoretical and experimental techniques for analyzing the optical gain, refractive index change, linewidth enhancement factor, and group index extracted from amplified spontaneous emission spectra of the plasmonic QD Fabry-Perot laser. First of all, we use the Hakki-Paoli method to extract the net modal gain. By changing the injection current, we obtain the change in the refractive index via wavelength shifts of Fabry-Perot peaks and the linewidth enhancement factor. We did the measurements under CW and pulsed mode operations to distinguish the amount of thermal effects. In the last part of this chapter, we show temperature-dependent threshold current of this device.

4.2   Theoretical Analysis of Modal gain, Refractive Index Change, Group Index, and Linewidth Enhancement Factor

4.2.1　Modal Gain

The Hakki-Paoli (HP) method is one of the most common method to extract net modal gain from amplified spontaneous emission (ASE) spectra. To derive the net modal gain, we first consider a semiconductor laser in a Fabry-Perot cavity, as shown in Fig. 4.1.

When a wave bounces back and forth in a Fabry-Perot cavity, its amplitude after one round trip of distance 2L has to remain at least the same to obtain gain.

$$1 = \sqrt{R_1 R_2} e^{GL} e^{i2k_0 n_e L}$$

(4.1)

where R_1 and R_2 are the reflectivities at the two facets of the Fabry-Perot cavity, G is the net modal gain, L is the cavity length, k_0 is the wave number, and n_e is the effective refractive index.

The real part of Eq. (4.1) is

$$\Gamma g = (1 - \Gamma)\alpha + \frac{1}{2L} \ln \frac{1}{R_1 R_2} = \alpha_i + \frac{1}{2L} \ln \frac{1}{R_1 R_2}$$

(4.2)

where Γ is the optical confinement factor. It determines the longitudinal mode spectrum of the Fabry-Perot laser. To obtain lasing action, the modal gain has to overcome the intrinsic loss α_i and the mirror loss $\alpha_m = \frac{1}{2L} \ln \frac{1}{R_1 R_2}$. Therefore, the threshold condition of the Fabry-Perot laser is

$$G_{th} = \Gamma g_{th} = \alpha_i + \frac{1}{2L} \ln \frac{1}{R_1 R_2}$$

(4.3)
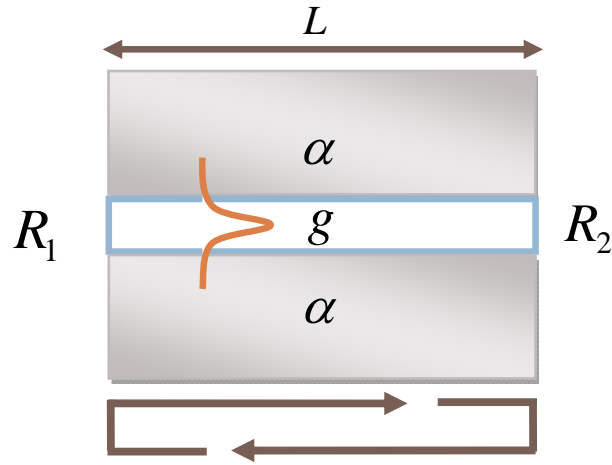
Fig 4.1 A simple modal of a Fabry-Perot cavity, which g is the optical gain in active region.

On the other hand, the imaginary part of Eq. (4.1) gives

$$2n_e L = m\lambda \tag{4.4}$$

When the phase-matching condition is satisfied, peaks of resonant Fabry-Perot modes are present in the ASE spectrum. Similarly, valleys of Fabry-Perot modes can be obtained from the antiresonance condition. Then, we can have the expression of amplified spontaneous emission for a Fabry-Perot laser [22]

$$I_{ASE}(\hbar\omega) = (1 - r_1 r_2)[\frac{W(\hbar\omega)L}{GL}]\frac{(e^{GL} - 1)(1 + r_1 r_2 e^{GL})}{|1 - r_1 r_2 e^{GL} e^{i2k_0 n_e L}|^2} \tag{4.5}$$

where $r_1 = \sqrt{R_1}$, $r_2 = \sqrt{R_2}$ are the electric field reflection coefficients of each facet. Since $1 - r_1 r_2 e^{GL} e^{i2k_0 n_e L}$ in the denominator is the only fast-varying term, it dominates the behavior of amplified spontaneous emission. As a result, we can approximate the slowly varying term in Eq. (4.2) with a constant K

$$I_{ASE}(\hbar\omega) = \frac{K}{|1 - r_1 r_2 e^{GL} e^{i2k_0 n_e L}|^2}$$

(4.6)

According to Eq. (4.6), field intensity $I_{ASE}(\hbar\omega)$ will reach its maximum when $e^{i2k_0 n_e L} = 1$, and

reaches its minimum when $e^{i2k_0 n_e L} = -1$. To make the arithmetic simpler, we define

$$S = \sqrt{\frac{I_{max}}{I_{min}}} = \frac{1 + r_1 r_2 e^{GL}}{1 - r_1 r_2 e^{GL}}$$

(4.7)

where I_{max} and I_{min} are the adjacent intensity maxima and minima of the FP modes,

respectively. After some manipulation, the net modal gain G can be extracted from the adjacent

peak and valley of the amplified spontaneous emission spectrum by

$$G = \frac{1}{L} \ln \frac{S-1}{S+1} + \frac{1}{L} \ln \frac{1}{r_1 r_2}$$

(4.8)

According to Eq. (4.8), several important parameters are obtainable. First, when the

wavelength is far larger from the gain region, modal gain Γg is approximately zero, so that net

modal gain would equal to material loss α_i, that is, $G = \Gamma g - \alpha_i = \alpha_i$. At or above threshold, G

will approach the mirror loss α_m, that is, $G = \Gamma g - \alpha_i = \alpha_m$, since $\sqrt{\frac{I_{max}}{I_{min}}}$ approaches to

infinity. By measuring the amplified spontaneous emission spectrum, both net modal gain and

material loss can be obtained.

4.2.2 Change of Refractive Index

The change in the refractive index, group index, and effective index can be extracted from the amplified spontaneous emission spectra. By considering adjacent longitudinal mode, FP mode spacing $\Delta\lambda_{FP}$ at single current bias is [20],

$$\Delta\lambda_{FP} = \frac{\lambda^2}{2L(n_e - \lambda\frac{\partial n_e}{\partial\lambda})}$$

(4.9)

From the waveguide theory, the group velocity v_g can be expressed as

$$v_g = \frac{n_g}{c} = \frac{\partial}{\partial\omega}(\frac{\omega}{c}n_e)$$

(4.10)

Since both n_e and λ are function of ω. The group index n_g can be expressed as

$$n_g = n_e - \lambda\frac{\partial n_e}{\partial\lambda}$$

(4.11)

From Eq. (4.9) and Eq. (4.11), we can get a compact expression for group index

$$n_g = \frac{\lambda^2}{2L\Delta\lambda_{FP}}$$

(4.12)

According to Eq. (4.1), we define λ_1 and λ_2 as two adjacent peak wavelength in ASE spectrum. The corresponding refractive indices are $n_{e1} = \frac{m_1\lambda_1}{2L}$ and $n_{e2} = \frac{m_2\lambda_2}{2L}$, respectively.

The change of the refractive index can be expressed as

$$\Delta n_e = n_e[\frac{\Delta\lambda}{\lambda} + \frac{\Delta m}{m}]$$

(4.13)

where $\Delta\lambda = \lambda_2 - \lambda_1$ and $\Delta m = m_2 - m_1$. Since the refractive indices are function of wavelengths and injection currents, the change of the refractive index can also be expressed as,

$$\partial n_e(\lambda, I) = \frac{\partial n_e(\lambda, I)}{\partial\lambda}\Delta\lambda + \frac{\partial n_e(\lambda, I)}{\partial I}\Delta I$$

(4.14)

Thus, manipulating of Eq. (4.13) and Eq. (4.14) gives

$$n_e \Delta\lambda m + \Delta m \lambda n_e - \lambda m [\frac{\partial n_e}{\partial \lambda} \Delta\lambda + \frac{\partial n_e}{\partial I} \Delta I] = 0$$

(4.15)

By substituting Eq. (4.9) into Eq. (4.15) and after some mathematical manipulation, we can obtain the induced change in the refractive index.

$$\Delta n_e = \frac{\lambda}{2L} \frac{\Delta\lambda_P}{\Delta\lambda_{FP}}$$

(4.16)

where $\Delta\lambda_p = \lambda_p(I_2) - \lambda_p(I_1)$ is the wavelength shift of FP peaks due to an increase in current injection. The equation is very useful to study the change in the refractive index from wavelength shifts of a single Fabry-Perot mode due to the change of injection current from I_1 to I_2.

4.2.3 Linewidth Enhancement Factor

Semiconductor lasers exhibit a strong variation of refractive index and net modal gain when injected carrier concentration changes. The parameter describing this dependency is called linewidth enhancement factor α_e [23]. The value of α_e is greatly important for many application of semiconductor lasers, such as laser linewidth, chirp, and response to optical feedback. Large values of α_e can result in a detrimental effect on a laser and can produce significant antiguidance, selffocusing, filamentation in broad-area emitters, and chirp under modulation. The increasing chirp will produce significant dispersion, which severely influences to high-speed signal processing in optical communications. As a result, minimization of α_e becomes a big issue for semiconductor lasers. For strained *InGaAs* single-quantum-well (QW) lasers which operate near 980 nm, a typical value of α_e has been shown to be 2 or higher at

carrier concentrations near threshold [24]. At the optical communication wavelengths of 1.3 and 1.55 μm, lasers exhibit usually significantly high value of α_e unless modulation doping [25] or multi-quantum-wells are employed in the laser device structure [26]. From the Kramers-Kronig relation, a symmetric gain profile will yield a zero α_e at the peak gain since the refractive index remains unchanged. Instead of QWs, the density of states of an ideal quantum dot (QD) has a series of delta-function at the quantized energy levels, indicating that ideal quantum dot lasers are expected to have reduced linewidth enhancement factor, which yields important impacts to optical communication area. A substantial reduction in α_e should be realized by using quantum dot lasers [27,28].

The linewidth enhancement factor α_e is defined as [29]

$$\alpha_e = \frac{\partial n^{'}}{\partial n^{''}}$$

(4.17)

where $n^{'}$ and $n^{''}$ are real and imaginary parts of refractive index, respectively. The complex propagation constant in the cavity is given by

$$k = k^{'} - i\frac{g}{2} = \frac{2\pi}{\lambda}(n^{'} - \frac{ig\lambda}{4\pi}) = \frac{2\pi}{\lambda}(n^{'} + in^{''})$$

(4.18)

Substituting Eq. (4.14) into Eq. (4.13) yields the linewidth enhancement factor

$$\alpha_e = -\frac{4\pi}{\lambda}\frac{\partial n_e}{\partial g} = -\frac{4\pi}{\lambda}\frac{\partial n_e / \partial N}{\partial g / \partial N}$$

(4.19)

where $\frac{\partial n_e}{\partial N}$ is the change in the refractive index due to the injected carrier changes, and $\frac{\partial g}{\partial N}$ is the change in the gain due to the injected carrier changes.

4.3 Net Modal Gain, Refractive Index Change, Linewidth Enhancement Factor, and Group Index of The QD Plasmonic Laser Under CW Mode Bias

This part presents the experimental data of the net modal gain, refractive index change, group index, and linewidth enhancement factor of the QD plasmonic laser under continuous wave (CW) mode bias. Those data are extracted from the amplified spontaneous emission spectra of the QD Fabry-Perot plasmonic laser. The emission spectrum falls on near-IR region (1200nm~1350nm).

4.3.1 Net Modal Gain

The QD Fabry-Perot laser is operated in CW mode bias to obtain the DC characteristics of the device. The reflectivities of each facet is estimated to be 0.299 by using the refractive index of $GaAs$ (n_{GaAs}=3.413 [30]). The cavity length is 1150 μm with error less than 0.5%. The ASE spectrum is obtained from incremental current injection of 2mA until the threshold condition of the laser is reached. The clear Fabry-Perot spectrum is evident when the emission intensity is strong enough compared to noise level. As the CW current increases, the gain increases to the amount offsetting the material losses and mirror loss. Above the threshold operation, the maximum modal gain is located at 1287 nm and the power density of the lasing modes are much higher compared with other longitudinal modes since stimulated emission has occurred. Further increase in the current injection will produce the lasing action of this device.
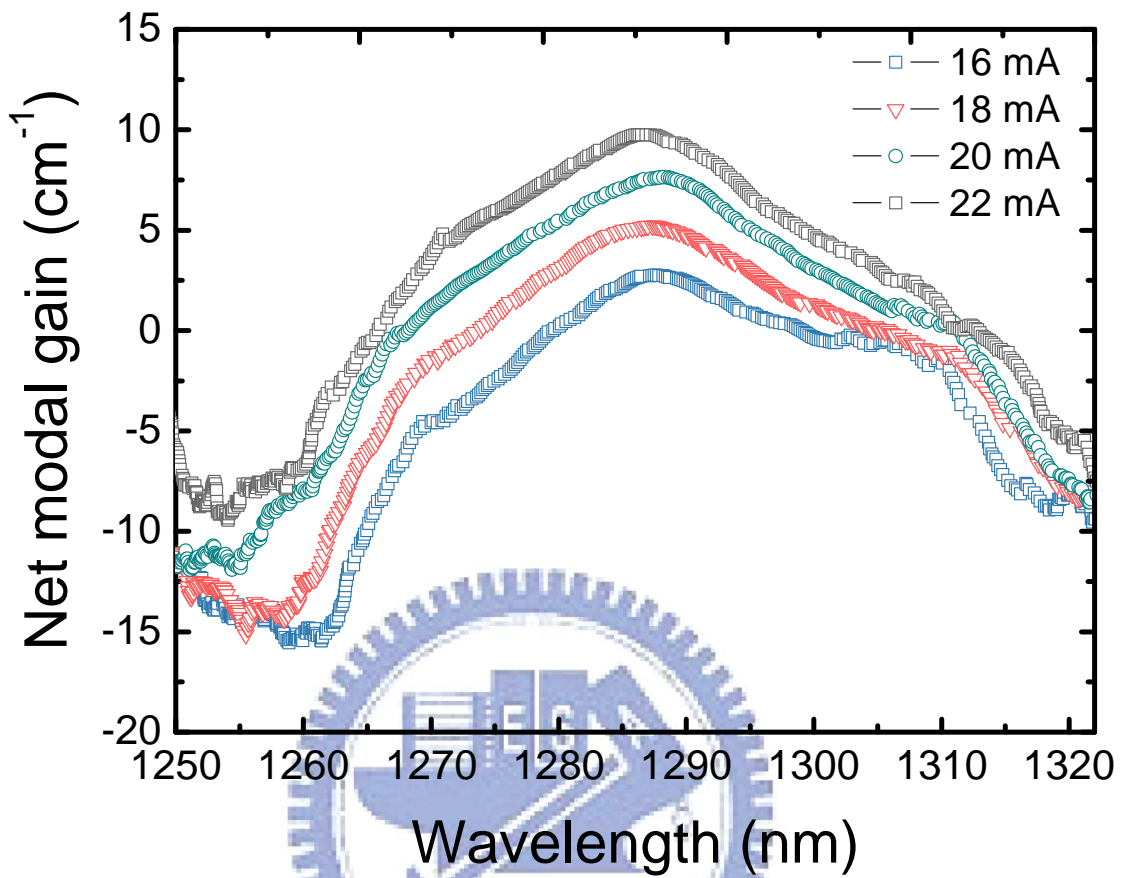
Fig 4.2 Current-dependent net modal gain extracted from the ASE spectra under CW current bias at 293 K.

Fig. 4.2 shows the current-dependent net modal gain of the QD laser under CW operation at 293K. The net modal gain is extracted from ASE spectra by using the Hakki-Paoli method. As the injection current increases, the net modal gain keeps growing until the laser reaches threshold condition. After lasing action takes place, the net modal gain is pinned and equals to the mirror loss, which is about 10.5 cm^{-1}. The plateau of the gain curves on the long wavelength side gives the intrinsic loss of the cavity medium, which is about 8 cm^{-1}. The threshold current of the QD

plasmonic laser is about 22.5 mA, corresponding to an carrier density of 0.978 kA/cm^2, which is comparably low as typical QD lasers.

It should be pointed out that the extraction of the net modal gain has its own difficulty on the longer or shorter wavelength side. The ASE spectrum covers certain wavelength range, and drops rapidly on both side. As the emission intensity is not large enough, insufficient signal-to-noise ratio (SNR) makes it difficult to obtain precise spectra and net modal gain.

4.3.2   Linewidth Enhancement Factor

Fig. 4.3 shows the ASE spectrum of the QD laser under CW current operation. Significant red shift of the Fabry-Perot modes is evident when injected current increases. Correspondingly, Fig. 4.4 shows the refractive index change extracted from the ASE spectra at two currents of 20mA and 22mA. It is clear to see the refractive index change is positive in magnitude in the emission range. With the change of refractive index and net modal gain change determined, linewidth enhancement factor can be extracted according to Eq. (4.19), as shown in Fig. 4.5. In the case of 20 mA and 22mA CW biasing, linewidth enhancement factor is always negative in the emission range from 1275 nm to 1295 nm. However, according to theoretical predictions, the refractive index change induced by external carrier injection should be negative and the linewidth enhancement factor should be positive. The obtained refractive index change and linewidth enhancement factor from the CW experiments show opposite magnitudes as theoretical predictions. Therefore, the observed phenomenon might be due to significant thermal effects from carrier heating.
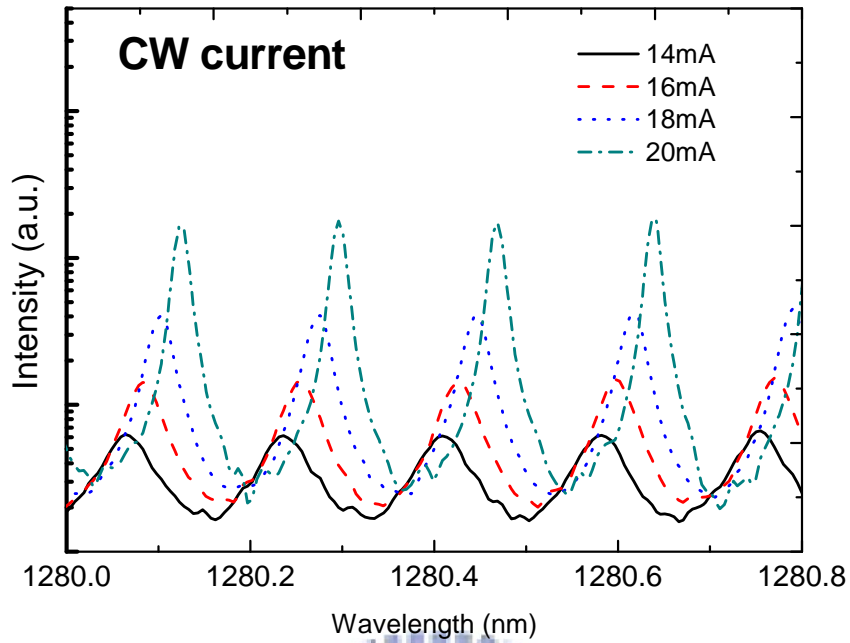
Fig 4.3 ASE spectra below threshold obtained of the QD laser biased in CW modes. Under CW current operation, significant red shift due to cavity heating from carrier injection is evident.
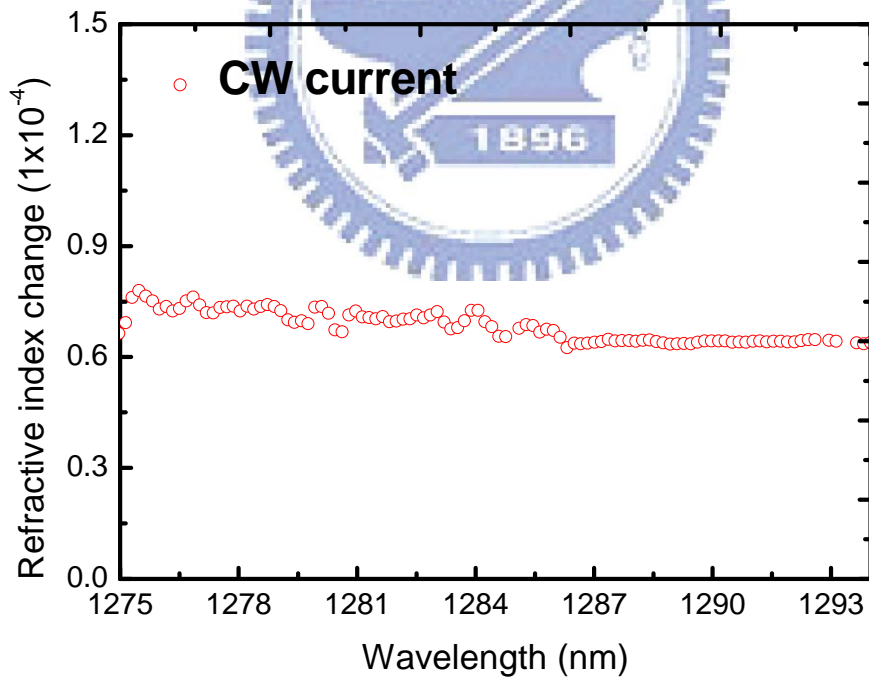
Fig 4.4 Refractive index change of the QD plasmonic laser under CW mode bias
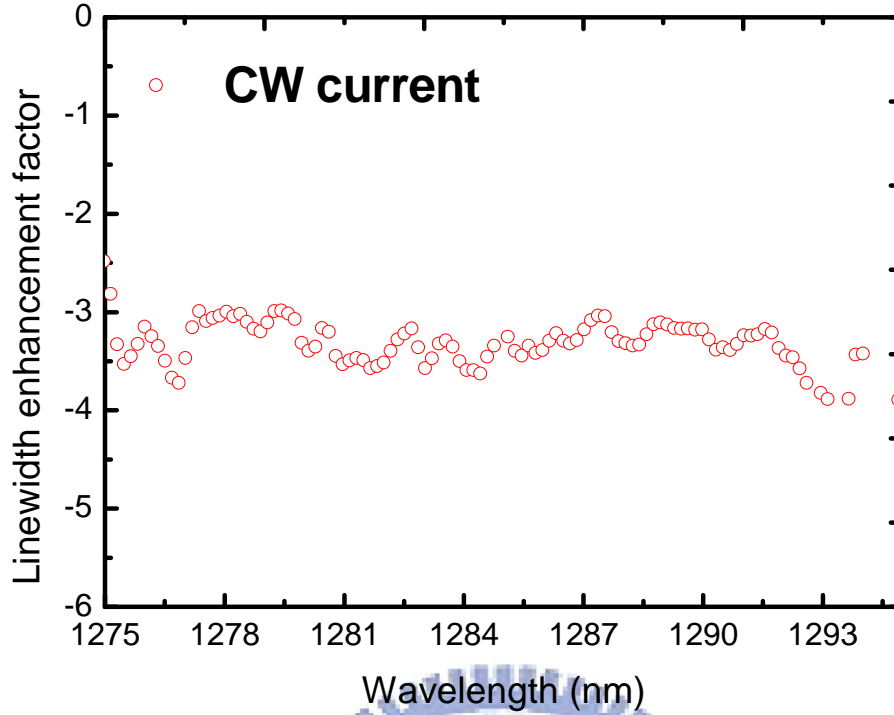
Fig 4.5 Linewidth enhancement factor of the QD plasmonic laser under CW mode bias

To isolate thermal effects, we will investigate the refractive index change as well as the linewidth enhancement factor under pulsed-current mode operation, where no significant thermal heating occurs. There will be more detailed discussions in Section 4.4.2.

4.3.3 Group Index

Fig. 4.6 shows the adjacent longitudinal mode FP mode spacing $\Delta\lambda_{FP}$ versus wavelength. The sharp features in the ASE peaks can facilitate the accurate determination of the peak position, and thus mode spacing. The spectra were recorded by the optical spectrum analyzer with resolution of about 5 pm. Hence the Fabry-Perot mode spacing of two adjacent Fabry-Perot peaks $\Delta\lambda$ is about 0.174 nm with errors small than 2.8%. The uncertainty of the group index at the two ends of the spectra is attributed to the insufficient signal-to-noise ratio of the emission intensity. Since

Fig 4.6 FP mode spacing versus wavelength of the QD plasmonic laser.

Fig 4.7 Measured group index spectrum extracted from the FP mode spacing. The group indices

in the emission range are around 4.2.

the group index was determined by Eq. (4.15), Fig. 4.7 plots the measured group index spectrum extracted from the multiple longitudinal Fabry-Perot interference peaks of ASE spectrum.

The measured group index are about 4.2, which are much larger than those of all possible materials of the QD laser, such as $GaAs$, $InGaAs$, and $AlGaAs$ in the emission region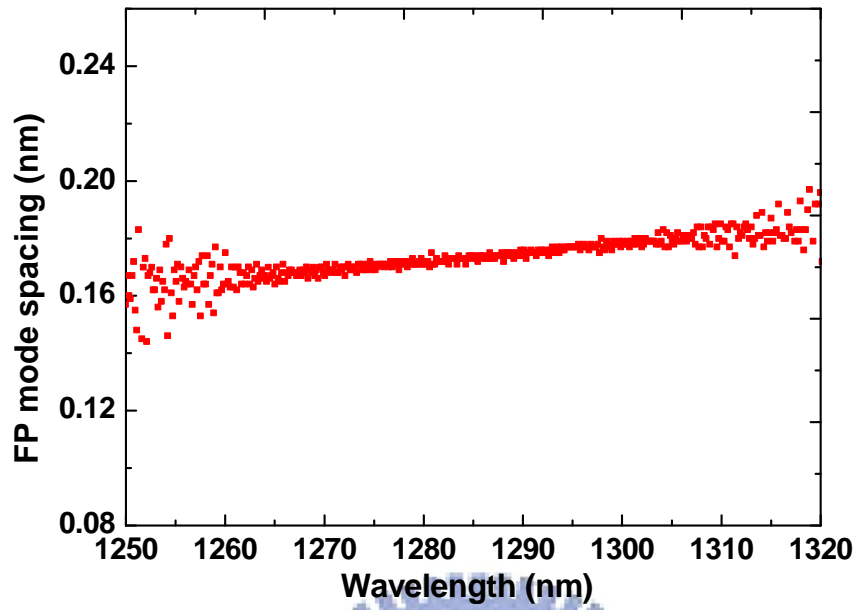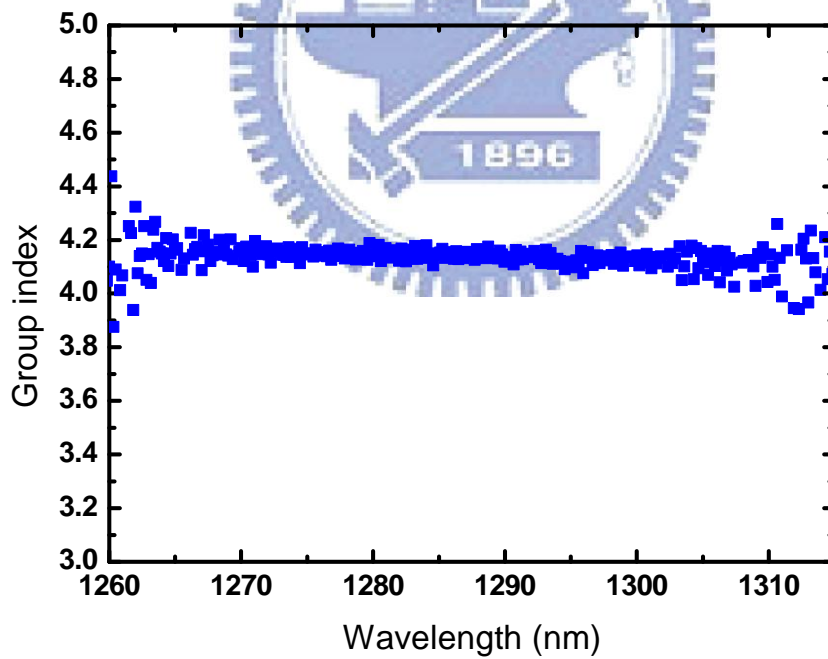 [30], Therefore, the high group index of about 4.2 indicate that the metallic waveguide influences the guided modes and therefore increases the group index.

4.4   Net Modal Gain, Refractive Index Change, linewidth Enhancement factor, and Group Index Under Pulsed Mode Bias

4.4.1   Net Modal Gain

To eliminate the thermal effects when operating the laser, we operate the device under pulsed current mode. Fig. 4.8 shows the measured ASE spectra of the QD plasmonic laser under pulsed current bias with a duty cycle of 2% and a pulsed width of $0.1\,\mu m$. As the injection current increases, the Fabry-Perot modes, as shown in Fig. 4.9, exhibits blue shift which is vividly opposed to the CW case presented in Fig. 4.3. This phenomenon is beacuse significant thermal effects have been eliminated under pulsed mode operation. The ASE spectrum is obtained from incremental current injection of 1mA until the threshold condition of the laser is reached. Fig. 4.10 shows the current-dependent net modal gain of the QD laser under pulsed mode operation at 293K. Compared to the CW case, the net modal gain depicted in here spans a

narrower spectral interval. The emission intensity of laser is lower under pulsed mode operation, and it consequences the change of gain shape. The threshold bias current is about 17mA under pulsed mode operation.

4.5.2   Linewidth Enhancement Factor and Group Index

In the case of pulsed mode bias, the change in the refractive index and linewidth enhancement factor are extracted from two current of 14mA and 15mA. The change in refractive index, as shown in Fig. 4.11. is always negative and the linewidth enhancement factor is always positive in the emission range, as opposed to the CW case, since thermal effects have been removed in the pulsed mode bias. The linewidth enhancement factor, as depicted in Fig. 4.12, at the lasing wavelength is as low as 0.35, which is much smaller than that in quantum well lasers (typical value is 2 or higher). Since the chirp parameter is propositional to $1+\alpha_e^2$, with this low linewidth enhancement factor, the reduced chirp in operation is possible for high speed optical communication applications.

Using the same analysis presented in Section 4.3.3 and Eq. (4.15), the group index can be extracted and shown in Fig. 4.13. The group indices under pulsed mode operation are roughly identical with those of the CW case, indicating the group index is not sensitive to temperature. Moreover, the measured group index are still much larger than typical $GaAs$ QD lasers.

In this section we have shown the measurements of amplified spontaneous emission spectrum, net modal gain, refractive index change, linewidth enhancement factor and group index under CW and pulsed mode operations. The symmetric gain shape is shown which yields a small linewidth enhancement factor. The obtained high group index of 4.2 is evident for the guided modes coupled to the metallic waveguide.
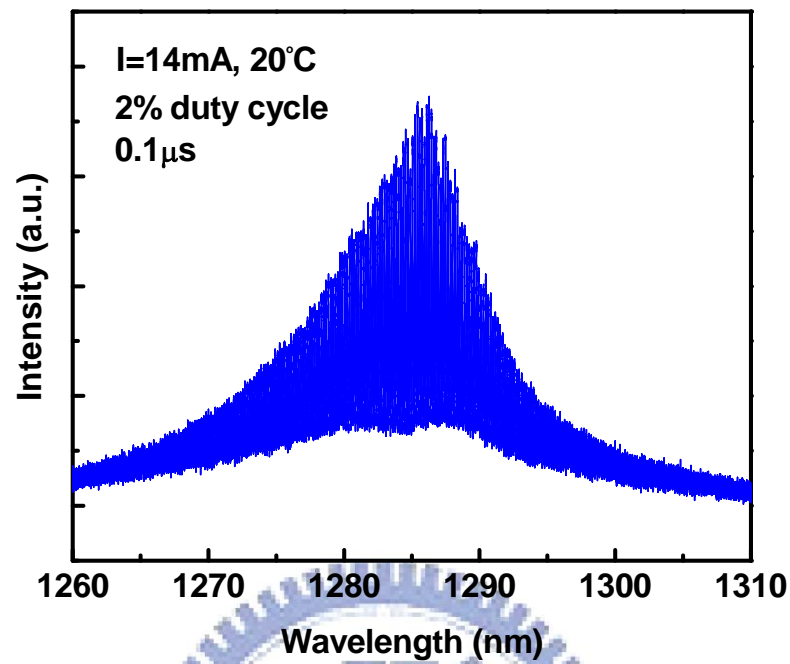
Fig 4.8 ASE spectrum under pulsed operation from the QD plasmonic laser.
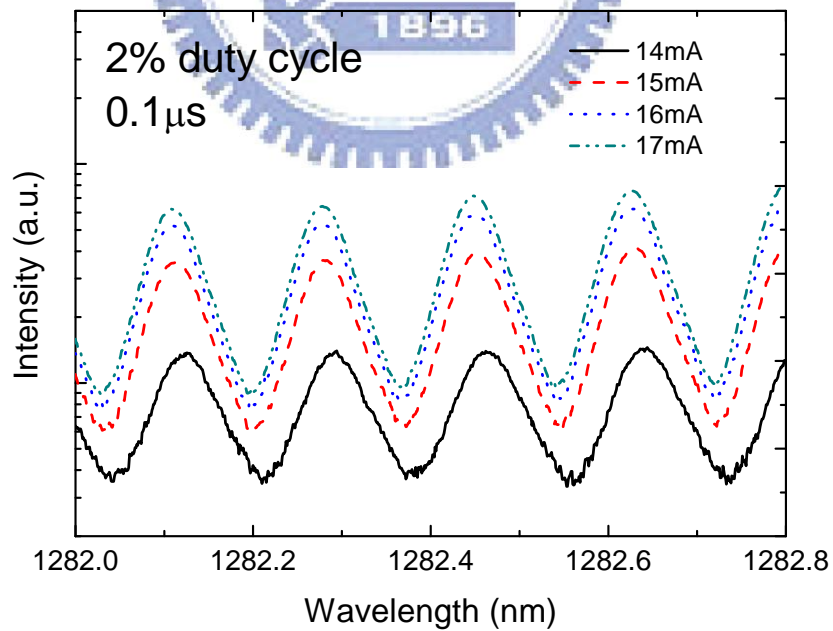
Fig 4.9 ASE spectra below threshold obtained of the QD laser biased in pulsed modes.
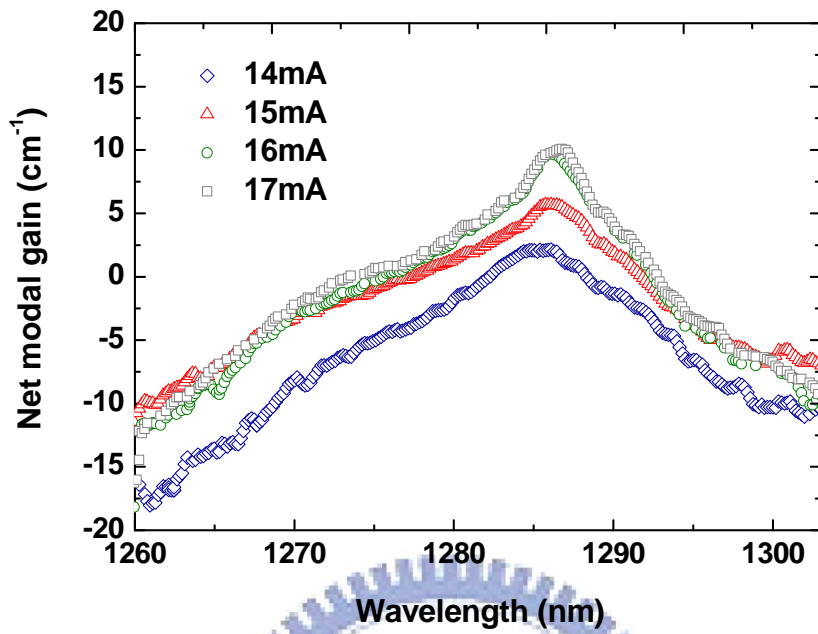
Fig 4.10 Current-dependent net modal gain extracted from the ASE spectra under pulsed current bias at 293 K.
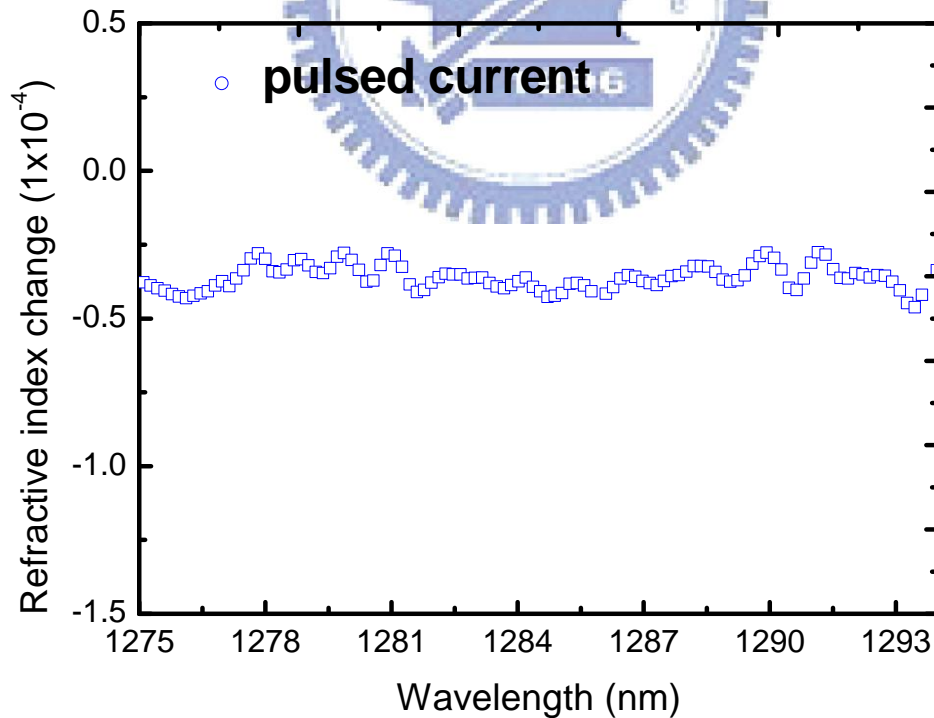
Fig 4.11 Induced Refractive index change by current increase of the QD plasmonic laser under pulsed mode bias
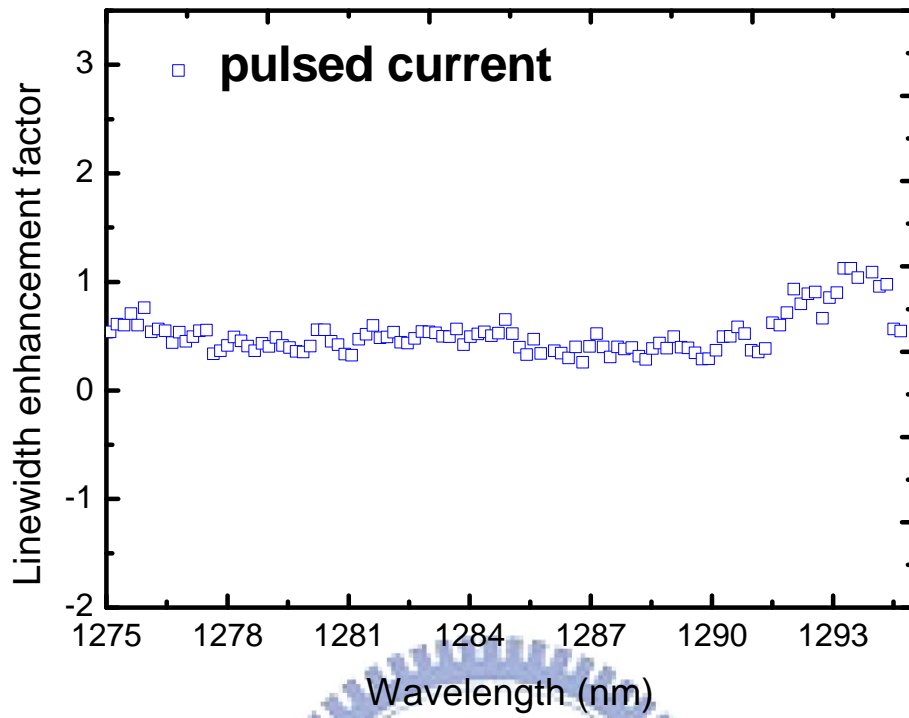
Fig 4.12 Linewidth enhancement factor of the QD plasmonic laser under pulsed mode bias
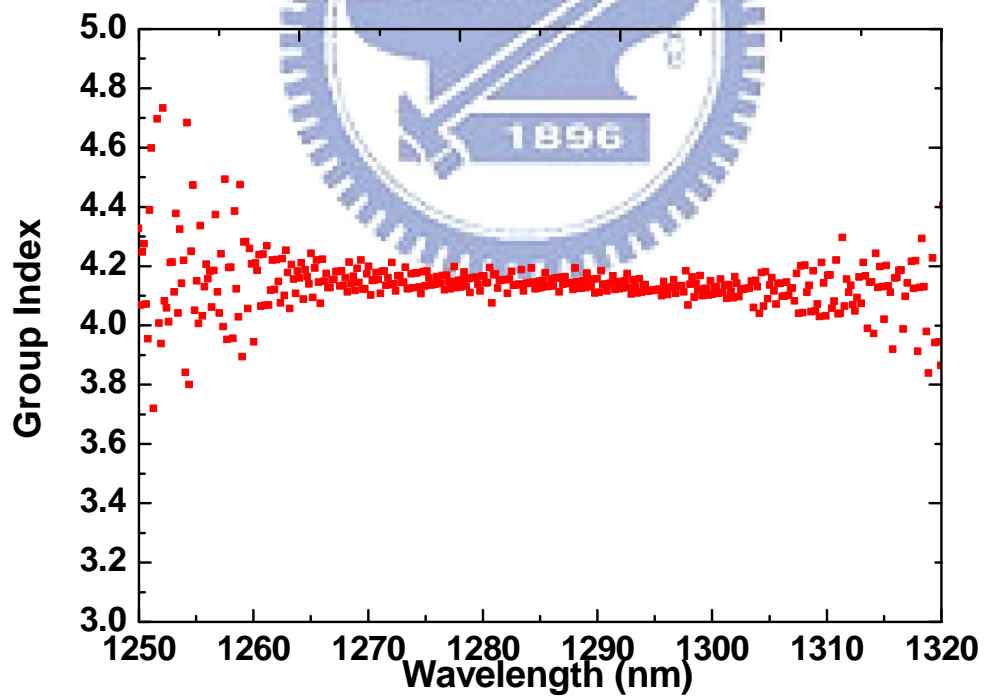
Fig 4.13 Measured group index spectrum extracted from the FP mode spacing under pulsed mode bias. The group indices in the emission range are around 4.15.

4.5 Temperature Dependance on QD FP Plasmonic Laser

4.5.1 Physics of Temperature Dependance

Lasing wavelength shift is an important characteristic of the laser since smaller dependence of temperature on the spectrum is desired for telecommunications. Since a commercial laser device is operated between a range of temperature, stability on the output is definitely an important issue in semiconductor laser researching area. A small spectral shift with temperature yields that a laser requires minimal even without using any cooling device. This would save some space in semiconductor integrated circuits and help the size minimization.

The temperature-dependent threshold current is also a very important parameter of semiconductor lasers. Lasers with highly temperature dependency of threshold current would cause unstable lasing condition when the operation temperature varies. This is definitely an undesirable property to set this device in the compact module system. Characteristic temperature is a parameter to quantify the thermal stability for threshold current of lasers under different temperatures. The characteristic temperature T_0 is defined as

$$T_0 = \frac{1}{\dfrac{\partial \ln J_{th}}{\partial T}}$$

$$J_{th} = J_0 e^{\frac{T}{T_0}} \tag{4.20}$$

where J_{th} is the threshold current density, J_0 is the normalization current density. From Eq. (4.20), low characteristic temperature indicates that threshold current density increases rapidly as the temperature increases. On the other hand, higher characteristic temperature implies that lasers are less sensitive to temperature induced by carrier injection. This translates into a laser being more thermal stable. One of the most important advantages of quantum dot semiconductor lasers

over quantum well or bulk lasers is the temperature-insensitivity of the threshold current density [17]. Ideal QD lasers have the property of an infinite characteristic temperature, which indicates a fixed threshold current density under unstable temperature condition [17]. However, fraction of free injection carrier spread into optical confinement layer in real situation. This would cause some carrier waste in the barrier region with recombination processes, and this associates through thermal excitation of carriers from quantum dots to other wavelengths which depends exponentially on temperature [31, 32, 33]. Therefore, characteristic temperature of real QD lasers should be finite, especially at high temperatures [34].

4.6.2   Measurement of Characteristic Temperature

The same current source (ILX LDC-3900) and thermo-electric-cooler controlled via Labview program is used to drive and sustains the temperature of the plasmonic QD laser. The optical power meter is used to collect light emission for intensity analysis and also can be controlled by Labview program.

The extracted T_0 under CW bias of the device is plotted in Fig 4.14. In the temperature range of 7-15^oC, infinity characteristic temperature is obtained, indicating complete temperature independence to the threshold current. The T_0 decreases to about 325 K in the temperature range of 15-25^oC, and to about 95 K in the temperature range of 25-40^oC, which might be attributed to an increase rate of Auger recombination as the temperature increases [35,36].

48
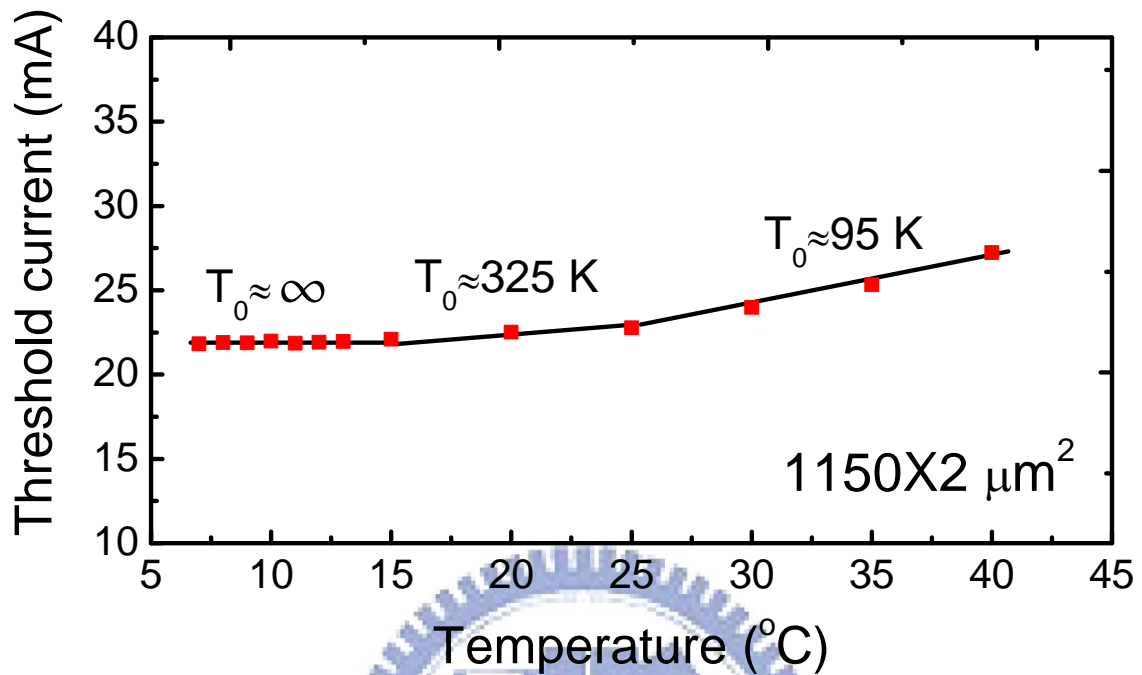
Fig. 4.14 Variation of threshold current with temperature. In the range of 7-15^oC the threshold current remains almost unchanged, resulting in an infinite characteristic temperature.

4.6 Conclusions

We have demonstrated a high performance QD Fabry-Perot laser with sidewall-coated metallic waveguide. We observed an infinite characteristic temperature in the range of 7-15^oC, indicating completely temperature-insensitive operation is possible. We have measured the ASE spectrum for extracting the net modal gain, the refractive index change, the linewidth enhancement factor, and the group index under CW and pulsed current bias operations. We observed significant red shift of ASE spectrum under CW current operation, which is believed owing to thermal effects.

By operating the laser in pulsed mode bias with low duty cycle to eliminate thermal effects, the ASE spectrum shows blue shift as opposite to the CW case, which yields positive magnitude in linewidth enhancement factor. The QD laser shows ultra small refractive index changes and linewidth enhancement factor in the emission range, leading reduced chirp in high speed operation. The measured high group index is evident for the guided modes coupled to the metallic waveguide.

CHAPTER 5

CONCLUSION

In conclusion, we have demonstrated a room-temperature comprehensive measurement of the plasmonic QD Fabry-Perot laser. We have shown the design of the QD plasmonic laser as well as the detailed fabrications. The metallic sidewall-coated laser was fabricated with the sample containing InAs/GaAs quantum dots as the active medium. After cleaving and mounting the device on the copper heat sink, we observed clear lasing action at room temperature. The cavity length of this device is $1150\,\mu m$ and the threshold current is 22.5mA under room temperature operation.

We then measured the amplified spontaneous emission spectrum, which allows to extract the net modal gain spectra, the change of refractive index, linewidth enhancement factor, and group index. Moreover, we have measured the laser under CW and pulsed mode bias to distinguish thermal effects from our experimental work. The change of refractive index and linewidth enhancement factor flip their sign to another by getting rid of carrier heating when the laser is operated in pulsed mode bias. Experimentally, infinite characteristic temperature is obtained at about 280K, which means our QD plasmonic laser has excellent thermal-stability properties. Ultra low linewidth enhancement factor of about 0.35 in the emission range is obtained and it indicates reduced chirp operation is possible for telecommunications. The observed high group

index in the QD laser with sidewall-coated metallic waveguide indicates that the metal contributes to the dispersion of the waveguide guiding mechanism.

In this thesis, we focus on the DC measurements of the QD plasmonic laser. However, it is also possible to measure the dynamic behaviors of the laser, such as relaxation frequency, damping factor, carrier lifetime, and theoretical maximum bandwidth. Also, constructing complete theoretical model would help comprehensively explore and understand the plasmonic effects in this device.

REFERENCES

[1] C. H. Fine, L. C. Kimerling, *Biography of a killer technology: Optoelectronics Drives Industrial Growth with the Speed of Light, in OIDA Future vision Program* (Optoelectronics Industry Development Association , Washington, DC 1997)

[2] W. L. Barnes, A. Dereux, and T. W. Ebbesen, Nature. **424**, 824 (2003)

[3] Hecht, B., Bielefeldt, H., Novotny, L., Inouye, Y. & Pohl, D. W., Phys. Rev. Lett. **77,** 1889 (1996).

[4] Pendry, J., Science **285,** 1687 (1999).

[5] Grakoui, A. et al., Science **285**, 221 (1999).

[6] Cambi, A. et al., J. Cell Bio. **164**, 145 (2004).

[7] Muhlschlegel, P., Eisler, H.-J., Martin, O. J. F., Hecht, B. & Pohl, D. W., Science **308**, 1607 (2005).

[8] Schuck, P. J., Fromm, D. P., Sundaramurthy, A., Kino, G. S. & Moerner, W. E., Phys. Rev. Lett. **94**, 017402 (2005).

[9] I. Abdulhalim, M. Zourob, A. Lakhtakia, Electromagnetics **28,** 214 (2008).

[10] Piner, R. D., Zhu, J., Xu, F., Hong, S. & Mirkin, C. A., Science **283**, 661 (1999).

[11] Srituravanich, W. *et al.*, Nature Nanotechnology **3,** 733 (2008).

[12] H. T. Miyazaki and Y Kurokawa, Phys. Rev. Lett. **9,** 097401 (2006)

[13] M. T. Hill, Y. Oei, B. Smalbrugge, Y. Zhu, T. De Vries, P. J. Van Veldhoven, F. W. M. Van Otten, T. J. Eijkemans, J. P. Turkiewicz, H. De Waardt, E. J. Geluk, S. Kwon, Y. Lee, R. Notzel, and M. K. Smit., Nat. Photon. **1,** 589 (2007)

[14] B. Min, E. Ostby, V. Sorger, E. Ulin-Avila, L. Yang, X. Zhang, and K. Vahala, Nature **457,** 455 (2009)

[15]Vitaly A. Shchukin, *Epitaxy of Nanostructures* (Springer, 2003), 1st ed.

[16] Z. Alferov, IEEE J. Select. Topics Quantum Electron. **6**, 832 (2000)

[17] Y. Arakawa and H. Sakaki, Appl. Phys. Lett. **40**, 939 (1982)

[18] R. Dingle and C. H. Henry, U.S. Patent 3 982 207 (1976).

[19] Kasap, Safa, *Handbook of Electronic and Photonic Materials* (Springer, 2007)

[20] S. L. Chuang, *Physics of Photonic Devices* (Wiley, New York, 2009), 2nd ed.

[21] J. Kim and S. L. Chuang, IEEE, *J. Quantum Electron*. **42,** 942 (2006)

[22] C. S. Chang, S. L. Chuang, J. R. Minch, W. W. Fang, Y. K. Chen, and T. Tanbun-Ek, IEEE J. Select. Topics Quantum Electron. **1**, 1100 (1995)

[23] C. H. Henry, IEEE J. Quantum Electron. **18**, 259 (1982)

[24] D. J. Bossert and D. Gallant, IEEE Photon. Technol. Lett. **8**, 322 (1996)

[25] P. A. Morton, D. A. Ackerman, G. E. Shtengel, R. F. Kazarinov, M. S. Hybertsen, T. Tanbunek, R. A. Logan, and A. M. Sergent, IEEE Photon. Technol. Lett. **7**, 833 (1995)

[26] H. R. Choo, B. H. O, C. D. Park, H. M. Kim, J. S. Kim, D. K. Oh, H. M. Kim, and K. E. Pyun, IEEE Photon. Technol. Lett. **10**, 645 (1998)

[27] M. Willatzen, T. Tanaka, Y. Arakawa, and J. Singh, IEEE J. Quantum Electron. **30**, 640 (1994)

[28] D. Bimberg, N. Kirstaedter, N. N. Ledentsov, Zh. I. Alferov, P. S. Kop'ev, and V. M. Ustinov, IEEE J. Select. Topics Quantum Electron. **3**, 196 (1997)

[29] T. C. Newell, D. J. Bossert, A. Stintz, B. Fuchs, K. J. Malloy, and L. F. Lester, IEEE Photon. Technol. Lett. **11**, 1527 (1999)

[30] E. D. Palik, *Handbook of Optical Constants of Solids* (Academic, New York, 1985).

[31] Miyamoto, Y., Miyake, Y., Asada, M., and Suematsu, Y., IEEE J. Quantum Electron. **25,** 2001 (1989)

[32] Asryan, L.v., and Suris, R.A., Semicond. Sei. Technol. **11***,* 554 (1996)

[33] Asryan, L.v., and Suris, R.A., IEEE J. Sel. Topics Quantum Electron. **3,** 148 (1997)

[34] Kirstaedter, N., Ledentsov, N.N., Grundmann, M. Bimberg, D., Ustinov, V.M., Ruvimov, S.S., Maximov, M.V., Kopev, P.S., Alferov, Zh. I., Richter, U., Werner, P., Gosele, U., and Heydenreich, J., Electron. Lett.*,* **30,** 416 (1994)

[35] B. W. Hakki and T. L. Paoli, J. Appl. Phys. **46,** 1299 (1975).

[36] J. Minch, S. L. Chuang, C.-S. Chang, W. Fang, Y.-K. Chen, and T. Tanbun-Ek, IEEE J. Quantum Electron., **33**, 815 (1997).